

Contents lists available at ScienceDirect

Journal of the Mechanics and Physics of Solids

journal homepage: www.elsevier.com/locate/jmps





Viscoelastic mechanics of two-dimensional granular lattices

Srinivas Selvaraju^a, Shailendra P. Joshi^{a,*}, Nikhil Karanjgaokar^b

- ^a Department of Mechanical Engineering, University of Houston, Houston, TX 77204-4006, USA
- ^b Department of Aerospace Engineering, Worcester Polytechnic Institute, Worcester, MA 01609-2280, USA

ARTICLE INFO

Keywords:
Granular lattices
Viscoelastic mechanics
Discrete element modeling
Porosity compaction & recovery

ABSTRACT

We study the rate-dependent mechanics of viscoelastic granular packings. Using a two-dimensional, square lattice of particles as a motif mimicking nominally mono-disperse granular packings, we perform a suite of finite element simulations under rate-dependent uniaxial compaction followed by unloading. The focus is on understanding the macroscopic force-displacement relations and the porosity evolution as a function of the viscoelastic relaxation parameters. For the constituent parameters considered here, the force-displacement relations show a two-stage power-law behavior, which is associated with the relative contributions of viscous dissipation and elastic effects at a particular loading rate. For a given loading rate, the nonlinearity of the porosity evolution depends on the constituent parameters and is found to be captured well by a simple analytical model. The heterogeneity of stresses during the compaction and recovery phases provide insights into the emergent complex micromechanics in simple granular motifs. Upon unloading, particles may experience transient tensile pressures, which could have implications on their failure.

1. Introduction

Soft granular assemblies are encountered in many natural systems (Kabla, 2012; Xu et al., 2019) and are important motifs in many engineered applications, from powder compaction (Jagota et al., 1998; Raps et al., 2015; Zhang et al., 2019) to pharmaceuticals and biosystems (Horabik and Molenda, 2016; Riley et al., 2019; Highley et al., 2019; Hirsch et al., 2021). Understanding the mechanical behaviors of such granular systems is essential for their translational applications (van Hecke, 2009; Menut et al., 2012; Li et al., 2021; Yuk et al., 2021).

In soft granular assemblies, the macroscopic force–displacement ($F-\Delta$) response is expected to be different from the classical Hertzian relation. For instance, compression experiments on spherical hydrogel granular assemblies in cubic lattice arrangements show $F \sim \Delta^{\beta}$ with $\beta = 2.2 \pm 0.2$ much larger than the Hertzian exponent of 1.5 (Brodu et al., 2015). The high deformability of individual particles has also been found to influence clogging with potential particle fracturing during their flow through silos (Ashour et al., 2017).

Sophisticated numerical approaches based on discrete element method (DEM) have been proposed to simulate macroscopic behaviors of highly deformable granular packings (Gonzalez and Cuitiño, 2012; Giannis et al., 2021). Using this approach it is found that even in simple lattice-type (square or hexagonal) granular arrangements the inter-particle force distribution and nonlocal effect are influenced by the type of arrangement and the mechanical property contrasts between individual particles (Li et al., 2021). DEM based analyses of two-dimensional granular systems comprising incompressible neo-Hookean particles indicate packing fraction (ψ) that varies nearly linearly with applied strain (Vu et al., 2019) and a contact relation $\langle Z \rangle \sim \psi^{\delta}$ where $\langle Z \rangle$ is the

E-mail address: shailendra@uh.edu (S.P. Joshi).

^{*} Corresponding author.

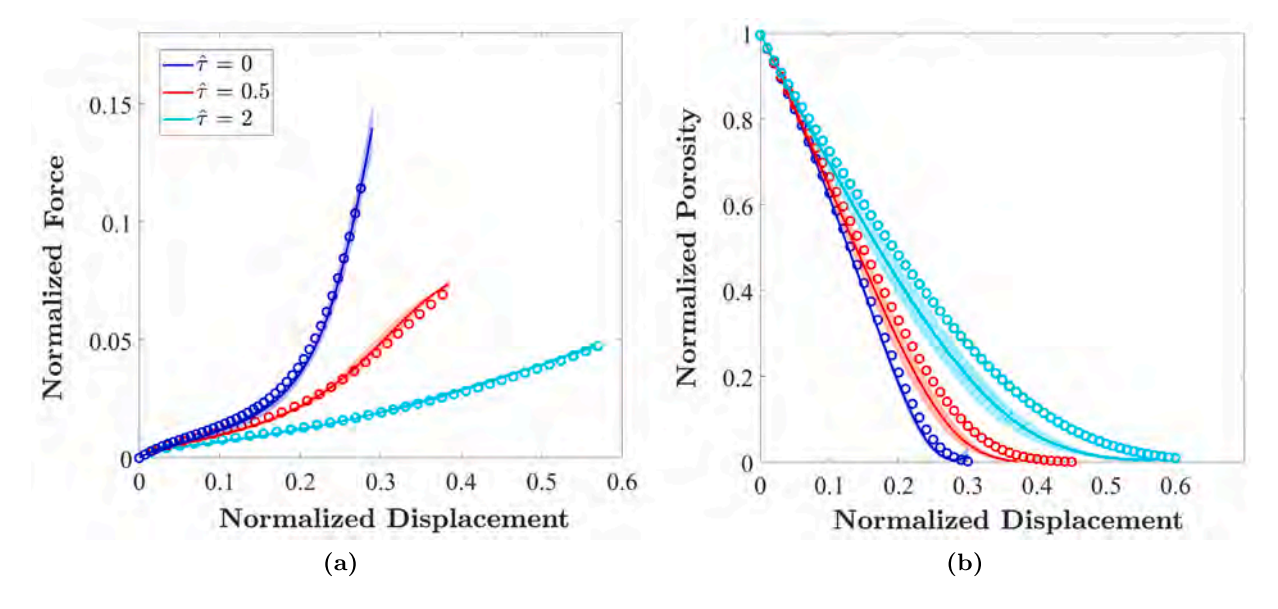


Fig. 1. Evolution of (a) normalized force and (b) porosity in randomly arranged mono-disperse granular packings (solid lines) for three viscoelastic materials (signified by parameter \hat{r} , discussed *et seq.*) under uniaxial strain rate of $\hat{\epsilon} = 0.03 \text{ s}^{-1}$. Shaded regions shows one standard deviation due to initial porosity variation (0.19 $\lesssim \phi_0 \lesssim 0.22$) due to diameter variations. Superposed on these results are the responses of square granular packings comprising particles with identical diameters (circles) and $\phi_0 = 0.2146$.

average number of contacts per particle and $\delta \sim 0.5$ (Cantor et al., 2020), which appears to corroborate with experiments (Vu et al., 2019). This is similar to the scaling observed in bubble models for wet foams (Durian, 1995) although somewhat different exponents have also been reported for compressible solid elastic particle assemblies (e.g., Makse et al., 2000). More recent DEM simulations of two-dimensional soft granular systems with compressible neo-Hookean particles (Vu et al., 2021) show that with increasing compressibility the packing fraction (ψ) evolves more slowly and becomes increasingly nonlinear with applied strain while the macroscopic stress–strain behavior becomes more compliant.

Often, the role of loading rate and its interaction with the material time-scales in deformable granular packings are of interest (Karanjgaokar, 2017; Kocharyan and Karanjgaokar, 2020). For instance, experiments on disordered hydrogel granular packings (Mukhopadhyay and Peixinho, 2011) show $F \sim \psi^{\beta}$ with a loading-rate dependent exponent values (1.2 $\lesssim \beta \lesssim$ 1.4) with the exponent decreasing with increasing loading rate. Interestingly, these exponents lie between those obtained for frictionless emulsions (~1.2) and frictional hard-sphere systems (~1.5). In the same experiments, the unloading response indicates that the recovery depends on the unloading velocity, which hints at the role of viscous dissipation processes. Such viscoelastic phenomena also occur in polymer powder compaction and sintering (Jagota and Dawson, 1988a,b; Jagota et al., 1998; Bellehumeur et al., 1998). It is understood that the mechanics of these systems is fundamentally rooted in the inter-particle interactions associated with viscoelastic contact mechanics (Graham, 1967; Shull, 2002). Yet, full-scale DEM-based simulations become important as complex multi-particle interactions can occur in such assemblies (McMeeking et al., 2001).

The focus of this work is on understanding the rate-dependent mechanics of viscoelastic granular packings. We use a finite element based DEM approach to simulate the compaction and recovery with an emphasis on the role of viscoelastic constituent properties. As an illustration, Fig. 1 shows the averaged (solid lines) normalized force–displacement responses (Fig. 1(a)) and normalized porosity (Fig. 1(b)) of randomly arranged granular packings with cylindrical particles of diameter $d_0 = 1.00 \pm 0.07$ mm following a normal distribution, which mimics experimental packings that are nominally mono-disperse (Mukhopadhyay and Peixinho, 2011; Brodu et al., 2015; Kocharyan and Karanjgaokar, 2020; Vu et al., 2021). The averaging is performed over five realizations with each realization comprising approximately 25–40 particles with fully periodic boundary conditions. Superposed in the figure are the responses (symbols) predicted by square packing modeled as a periodic unit cell (cf. Fig. 2) with $d_0 = 1.00$ mm. Notably, the square packing reasonably mimics the qualitative and quantitative trends of such nominally mono-disperse packings. Motivated by this, we consider a simple computational system comprising a granular lattice with particles arranged in square packing to study the deformation behaviors under nominally uniaxial straining.

Section 2 describes the basic computational set up and key theoretical ingredients. Section 3 analyzes the role of the dissipative and elastic effects on the macroscopic force–displacement and porosity (packing) evolution. In Section 4, we present an analytical model for porosity evolution. Section 5 presents an extended discussion of the results with insights into the role of packing architecture and the influence of constituent parameters in porosity recovery during unloading.

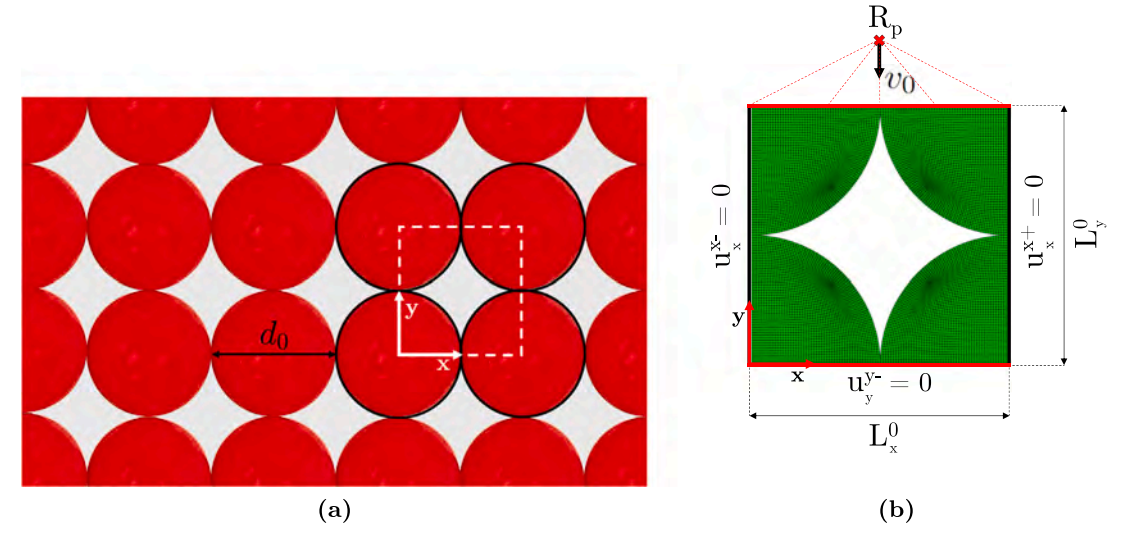


Fig. 2. (a) Illustrative real image of a square granular lattice comprising soft polymer particles, and (b) unit cell used in the calculations.

2. Model description

2.1. Geometry

Fig. 2(a) shows a two-dimensional square lattice comprising an infinite array of viscoelastic cylindrical particles of diameter $d_0 = 1$ mm. We assume a plane strain condition in the z-direction. In this configuration, the initial porosity $\phi_0 = 0.2146$. Fig. 2(b) shows the corresponding unit cell with the periodic boundary conditions. The unit cell is discretized using $\sim 10,000$ eight-node hybrid plane strain finite elements with linear pressure (CPE8H) in ABAQUS/STANDARD®. The model incorporates general periodic boundary conditions on the cell edges using multi-point constraint equations as follows (Garoz et al., 2019):

$$u_i^{i+} - u_i^{i-} = \epsilon_{ii}^0 L_i^0 \tag{1}$$

where ϵ^0_{ij} is the applied (nominal) strain on the cell, L^0_i the initial length of unit cell in the ith direction between opposite surfaces. Motivated by uniaxial deformation states investigations in the deformation behaviors of soft granular media (Mukhopadhyay and Peixinho, 2011; Dijksman et al., 2013; Vu et al., 2021), we focus on the response of granular packings subjected to a uniaxial applied strain. With reference to Fig. 2(b), a compressive velocity v_0 is applied in the y-direction at R_p (which acts as a loading device) so that $\epsilon^0_{yy}(t) \equiv \bar{\epsilon} = v_0 t / L^0_y$. Further, we prescribe $u^{y-}_y = 0$. Finally, with out-of-plane deformation constrained to zero, a uniaxial strain state is maintained by prescribing $u^{x+}_x = u^{x-}_x = 0$, which also ensures symmetry along the x-axis.

We consider 0.03 mm/s $\leq v_0 \leq 1$ mm/s; with $L^0_x = L^0_y = 1$ mm the investigation is carried out over a nominal strain rate range of 0.03 s⁻¹ $\leq \bar{\epsilon} \leq 1$ s⁻¹. The inter-particle contact interaction is defined using a general surface–surface contact in

We consider 0.03 mm/s $\leq v_0 \leq 1$ mm/s; with $L_x^0 = L_y^0 = 1$ mm the investigation is carried out over a nominal strain rate range of 0.03 s⁻¹ $\leq \dot{\varepsilon} \leq 1$ s⁻¹. The inter-particle contact interaction is defined using a general surface–surface contact in ABAQUS/STANDARD[®]. The pressure-overclosure relationship (normal contact) is modeled using hard contact (default), which minimizes the inter-surface penetration. It also does not allow the transfer of tensile stress across the interface. The tangential contact is modeled with a Coulomb friction formulation with friction coefficient, $\mu = 0.1$. As shown in Fig. S1 of the Supplementary Material, the friction coefficient has no measurable effect on the response of the granular system considered in this work.

2.2. Brief theoretical background

The present problem is studied in a large strain setting while the underlying rheological behavior is linear viscoelastic, commonly referred to as finite linear viscoelasticity (Coleman and Noll, 1961; Lubliner, 1985; Wineman, 2009). We lay out the basic framework as described in the ABAQUS® Theory Manual (Section 4.8.2 in Version 6.14) but the reader is also referred to Simo (1987) and Simo and Hughes (2006) for details; here, temperature effects are not considered.

For a compressible linear viscoelastic material, the second Piola–Kirchhoff stress is assumed to be additively split into a volumetric part and a deviatoric part in the reference configuration. The former is a function of $J(t) = \det \mathbf{F}(t)$ where $\mathbf{F}(t)$ is the deformation gradient at time t while the latter depends on the distortional gradient, $\mathbf{F} = \mathbf{F}/(J^{1/3})$, which is volume-preserving. Using push-forward

¹ ABAOUS®, User Documentation 2018, Dassault Systemes, RI, USA, 2018.

approach (Simo and Hughes, 2006) the hereditary integral in the current configuration relates the deviatoric ($\tau^{D}(t)$) and hydrostatic ($\tau^{H}(t)$) stress responses to deformation at time t as²:

$$\boldsymbol{\tau}^{D}(t) = \boldsymbol{\tau}_{0}^{D}(t) + \text{dev}\left[\int_{0}^{t} \frac{\dot{G}(s)}{G_{0}} \bar{\mathbf{F}}_{t}^{-1}(t-s) \cdot \boldsymbol{\tau}_{0}^{D}(t-s) \cdot \bar{\mathbf{F}}_{t}^{-\mathsf{T}}(t-s) ds\right]$$
(2a)

$$\tau^{H}(t) = \tau_{0}^{H}(t) + \int_{0}^{t} \frac{\dot{K}(s)}{K_{0}} \tau_{0}^{H}(t-s) ds$$
 (2b)

where $\tau_0^{\rm D}$, $\tau_0^{\rm H}$ are respectively the instantaneous deviatoric and hydrostatic contributions of the Kirchhoff stress τ_0 and s is a dummy variable that accounts for the history effects. G_0 and K_0 are the instantaneous (at t=0) small strain shear and bulk moduli, respectively and \dot{G} and \dot{K} are the time-derivatives of the small strain shear (G(t)) and bulk (K(t)) relaxation moduli. In Eq. (2a), the deviator operator in the current configuration is given as $\text{dev}[\circ] \equiv [\circ] - (1/3)[(\circ): I]I$ where I is the identity tensor. In ABAQUS[®], the relaxation moduli are expressed in non-dimensional forms. Following that, in the present work we assume the shear and bulk relaxation functions as follows:

$$g(t) = 1 - g_1 \left(1 - e^{-t/\tau_g} \right)$$
 ; $k(t) = 1 - k_1 \left(1 - e^{-t/\tau_k} \right)$ (3)

where $g_1 = 1 - (G_{\infty}/G_0)$ and $k_1 = 1 - (K_{\infty}/K_0)$, G_{∞} and K_{∞} are the long-term (relaxed) moduli, and τ_g and τ_k the corresponding relaxation time-scales. A rheological representation of these relaxation functions is a standard linear solid comprising a linear spring in parallel with a Maxwell element. The material is linear in the sense that g(t) and k(t) are not functions of strain (cf. ABAQUS[®] User's Manual, Version 6.14). Substituting Eq. (3) in Eq. (2), we obtain:

$$\boldsymbol{\tau}^{\mathrm{D}}(t) = \boldsymbol{\tau}_{0}^{\mathrm{D}}(t) - \det \left[\frac{g_{1}}{\tau_{n}} \int_{0}^{t} \bar{\mathbf{F}}_{t}^{-1}(t-s) \cdot \boldsymbol{\tau}_{0}^{\mathrm{D}}(t-s) \cdot \bar{\mathbf{F}}_{t}^{-\mathrm{T}}(t-s) \mathrm{d}s \right]$$
(4a)

$$\tau^{H}(t) = \tau_{0}^{H}(t) - \frac{k_{1}}{\tau_{t}} \int_{0}^{t} \tau_{0}^{H}(t-s) ds$$
 (4b)

Fig. S2 in Supplementary Material illustrates the role of finite deformation in the response of a linear visco-elastic material. In what follows, we define the following ratios: $\hat{G} = G_0/G_\infty$, $\hat{K} = K_0/K_\infty$ (the relaxation modulus ratios), and $\hat{\tau} = \tau_g/\tau_k$ (timescale contrast). We choose $10^0 \lesssim \hat{G} \lesssim 10^2$ ($\hat{G} \in \{1.5, 3.5, 11.5, 31.5, \text{ and } 85.5\}$) where $\hat{G} = 85.5$ is representative of polyurethane with $G_\infty = 5.607$ MPa, $G_0 = 477.6$ MPa (Kocharyan and Karanjgaokar, 2020). Further, we assume $\hat{K} = \hat{G}$, which is reasonable for several polymeric materials (Leaderman, 1958; Theocaris, 1965; Yee and Takemori, 1982; Shireen et al., 2023). Here, K_0 is computed via Hooke's law by taking instantaneous Poisson's ratio, $v_0 = 0.4$ (Karpiesiuk, 2020). Thus, for $\hat{K} = 85.5$, $K_\infty = 26.162$ MPa, $K_0 = 2226.83$ MPa. In terms of Eq. (3), $\hat{G} = \hat{K} = 85.5$ translates to $g_1 = k_1 = 0.988$. For simplicity, we take a fixed value of $\tau_g = 0.55$ s and vary τ_k to obtain $0 \le \hat{\tau} \le 10$ ($\hat{\tau} \in \{0, 0.5, 1, 2, \text{ and } 10\}$). As $\hat{\tau}$ describes the relative strength of shear relaxation mechanisms to the bulk relaxation mechanisms, we refer to materials with $\hat{\tau} < 1$ as shear relaxing materials as the shear relaxation is faster than the bulk relaxation despite $\hat{K} = \hat{G}$. By extension, materials with $\hat{\tau} > 1$ are referred to as bulk relaxing materials and those with $\hat{\tau} = 1$ as equi-relaxing materials. The $\hat{\tau}$ range is relevant to engineered polymers. For instance, linear polymers such as polycarbonate and polystyerene show $\hat{\tau} \gg 1$ whereas cross-linked polymers show $\hat{\tau} \lesssim 1$ (Grassia et al., 2010). Fig. A.1 in Appendix A show shear (Fig. A.1(a)) and bulk (Fig. A.1(b)) relaxation moduli for two illustrative values of \hat{G} .

3. Results and discussion

In this section, we describe the interaction between the loading time-scale $(t_L = 1/\dot{\epsilon})$ and the material time-scale $(\hat{\tau})$, and the role of the relaxation modulus ratios $(\hat{G}(=\hat{K}))$ in this interaction. Our focus is on understanding the force–displacement and the porosity evolution characteristics.

3.1. Force-displacement responses

We define the normalized force $(\bar{\sigma}(t))$ and the normalized displacement $(\bar{\Delta}(t))$ at time t:

$$\bar{\sigma}(t) = \frac{1 - (v(t))^2}{E_0} \left[\frac{F(t)}{A_0} \right]; \qquad \bar{\Delta}(t) = \frac{\Delta(t)}{L_v^0}$$
 (5)

where F(t) is the total macroscopic force in the loading direction acting on the initial unit cell area A_0 , E_0 the instantaneous Young's modulus, v(t) the time-dependent Poisson's ratio (see Eq. (A.1), Fig. A.1(c)) and $\Delta(t) = v_0 t$ the applied displacement. Fig. 3 shows that the $\bar{\sigma} - \bar{\Delta}$ responses are rate-dependent and nonlinear for the range of $\hat{\tau}$ ratios. At a given strain rate, as the role of the bulk relaxation time-scale becomes important (i.e., with increasing $\hat{\tau}$) the response becomes more compliant. The increased compliance with increasing $\hat{\tau}$ is seen at all three strain rates. At a given $\hat{\tau}$, the response becomes stiffer with increasing strain rate ($\hat{\epsilon}$). While Fig. 3 is shown for $\hat{G}=85.5$, the same features are observed for other relaxation modulus ratios (\hat{G}), cf. Fig. B.1 in Appendix B. In addition, Fig. B.1 shows that with increasing \hat{G} the normalized force (for a fixed $\hat{\tau}$ and $\hat{\epsilon}$) is lower, which is expected given the stronger stress relaxation.

² A^{-1} is the inverse of tensor A and A^{-T} is the transpose of A^{-1} .

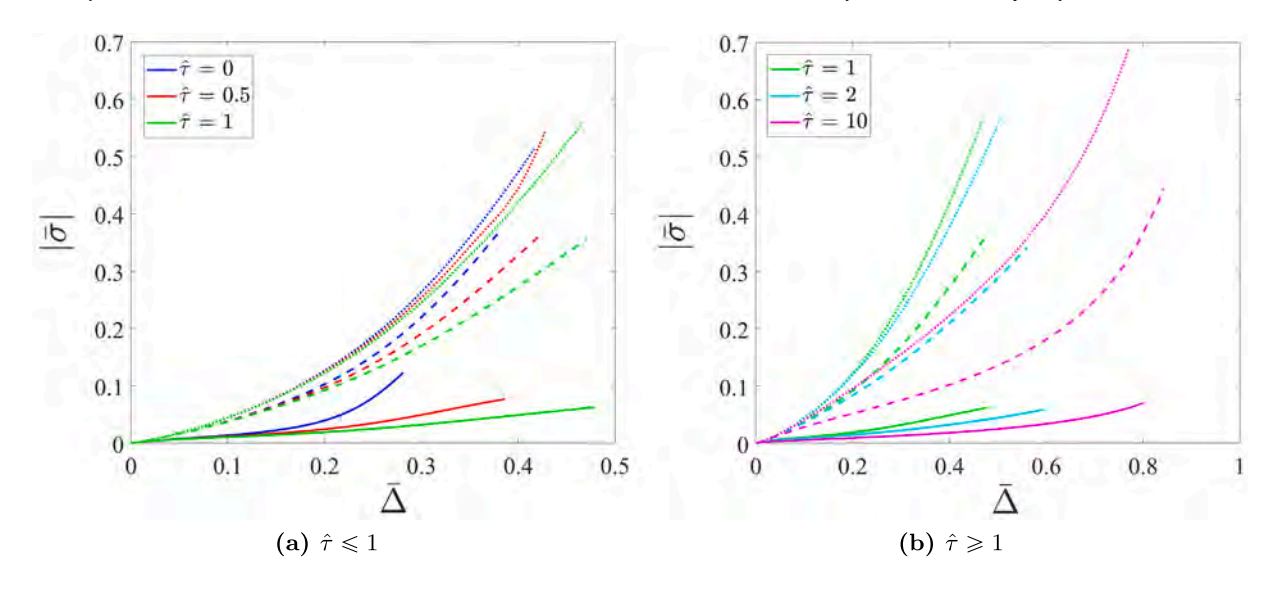


Fig. 3. Normalized force-normalized displacement $(\bar{\sigma} - \bar{\Delta})$ responses for $\hat{G} = 85.5$ for different $\hat{\tau} - \hat{\varepsilon}$ combinations. $\hat{\varepsilon} = 0.03 \text{ s}^{-1}$ (----) and $\hat{\varepsilon} = 1 \text{ s}^{-1}$ (-----).

It is pertinent to ask: Why does the $\bar{\sigma}-\bar{\Delta}$ response become more compliant with increasing $\hat{\tau}$? For a shear relaxing material $(\hat{\tau}\ll 1)$ the particles effectively behave as if they are less compressible as evidenced from the Poisson's ratio (Fig. A.1(c)), which may tend toward the incompressibility limit. As a result, the overall force required by the granular system to accommodate an applied deformation $(\bar{\Delta})$ is dictated by the hydrostatic stress as the deviatoric stresses relax. This effect, although present in the case of a single particle, is compounded in a granular system due to the confinement from neighboring particles. In comparison, a bulk relaxing material $(\hat{\tau}\gg 1)$ experiences much faster relaxation of the hydrostatic stresses and the deviatoric stresses also relax (given the fixed value of the shear relaxation time-scale, τ_{ν}). As a result, the larger the $\hat{\tau}$ the lower the overall force.

In both scenarios, the strong stiffening effect occurs when the porosity is sufficiently low, which occurs earlier in the case of a shear relaxing granular lattice compared to a bulk relaxing granular lattice. The effect of relaxation parameters in porosity evolution is discussed in Section 3.2.

We find that the normalized force-displacement responses are best described by the following relation:

$$\bar{\sigma} = \begin{cases} S_0 \bar{\Delta}^{\beta_0}, & \text{if } \bar{\Delta} \leq \bar{\Delta}_{\text{th}} \\ S_1 \bar{\Delta}^{\beta_1}, & \text{if } \bar{\Delta} > \bar{\Delta}_{\text{th}} \end{cases}$$

$$(6)$$

where \bar{A}_{th} is a threshold normalized displacement delineating two regimes described by the scaling exponents β_0 or β_1 . These regimes are discovered by considering the ratio $\mathcal{E} = \mathcal{D}_{visc}/\mathcal{W}_{elastic}$ in our analysis, which indicates the relative contributions of the viscous dissipation (\mathcal{D}_{visc}) and stored strain energy ($\mathcal{W}_{elastic}$).

Fig. 4 illustrates how \mathcal{E} evolves with $\bar{\Delta}$ for $\hat{G}=85.5$. At $\dot{\hat{\epsilon}}=0.03~{\rm s}^{-1}$ (solid lines in Fig. 4), all curves exhibit a non-monotonic trend with \mathcal{E} reaching a peak value ($\mathcal{E}_{\rm peak}>1$). It indicates that the viscous dissipation effect dominates during the initial part of the loading process while there is an increasing role of elasticity beyond the peak.

With increasing strain rate, the evolution of \mathcal{E} ratio with $\hat{\tau}$ is more complicated. At the high strain rate of $\dot{\varepsilon}=1.0~\text{s}^{-1}$ (dotted lines in Fig. 4), elastic effects dominate ($\mathcal{E}\ll 1$) in all cases, except for $\hat{\tau}=10$ where it marginally exceeds one. The dominant elastic contribution is not entirely unexpected as time scales for the shear and bulk dissipative processes may be too large to contribute significantly. At the intermediate strain rate ($\dot{\varepsilon}=0.3~\text{s}^{-1}$, dashed lines in Fig. 4), the trends are mixed. Here, the viscous effect tends to be dominant in equi- and bulk-relaxing materials ($\hat{\tau}\gtrsim 1$) with secondary contribution from elasticity. In comparison, elastic contributions dominate for shear-relaxing cases ($\hat{\tau}<1$). Although not shown here, we find that at $\dot{\varepsilon}=0.3~\text{s}^{-1}$ these trends are observed only for $\hat{G}\gtrsim 11$, i.e., for materials with sufficiently large contrast between the instantaneous and long-term moduli.

From these characteristics, we identify $\bar{\Delta}_{th}$ as the threshold displacement corresponding to \mathcal{E}_{peak} . We refer to the β_0 regime $(\bar{\Delta} \leq \bar{\Delta}_{th})$ as the dissipation-governed regime and the β_1 regime $(\bar{\Delta} > \bar{\Delta}_{th})$ as the elasticity-governed regime.

Fig. 5 summarizes the dependence of the two-regime behavior over the range of material parameters in terms of \bar{A}_{th} . The trends signify that for a given relaxation time-scale ratio $(\hat{\tau})$ increasing the relaxation modulus ratio (i.e., \hat{G}) delays the transition from a dissipation-governed behavior to an elasticity-governed behavior. The relaxation time-scale ratio $(\hat{\tau})$ starts playing a role at relatively modest levels of \hat{G} (\gtrsim 3.5). For $\hat{\tau} > 0$, the threshold displacement decreases with increasing $\hat{\tau}$. This can be interpreted as follows. Given that $\hat{\tau}$ is varied by varying τ_k while keeping τ_g is fixed, this dependence (at a given $\hat{\epsilon}$ and \hat{G}) is essentially a consequence of

³ In ABAQUS/STANDARD®, these are respectively the output variables ALLCD and ALLSE.

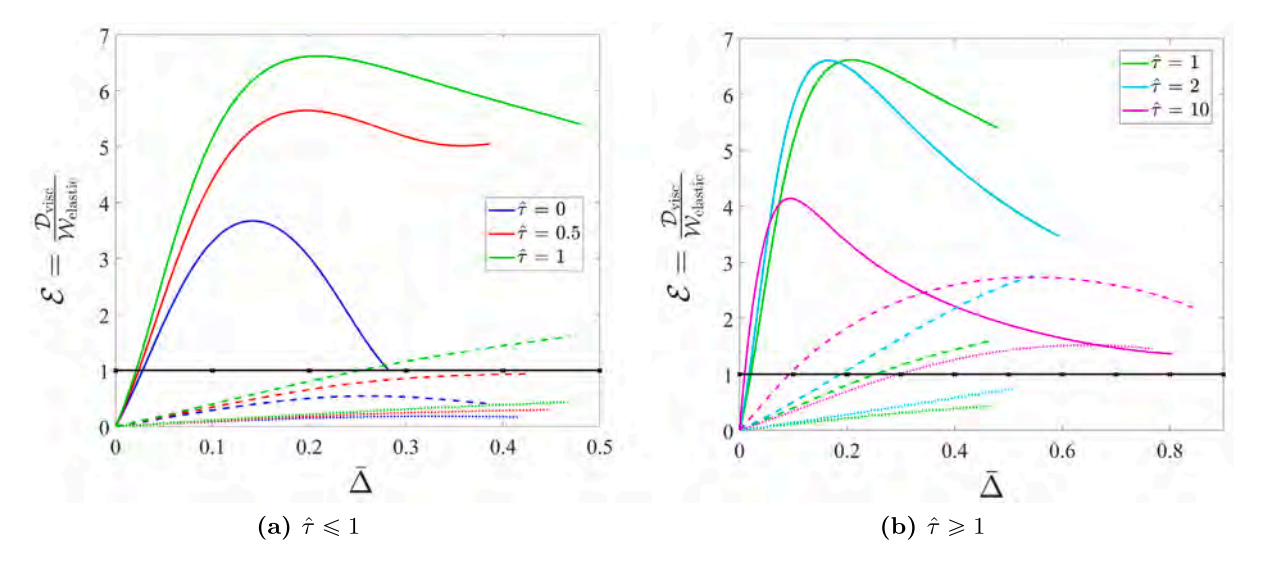


Fig. 4. Evolution of the ratio \mathcal{E} for different $\hat{\tau} - \dot{\bar{\varepsilon}}$ combinations (for $\hat{G} = 85.5$), where $\dot{\bar{\varepsilon}} = 0.03 \text{ s}^{-1}$ (---) and $\dot{\bar{\varepsilon}} = 1 \text{ s}^{-1}$ (----). Similar trends are observed for other \hat{G} ratios.

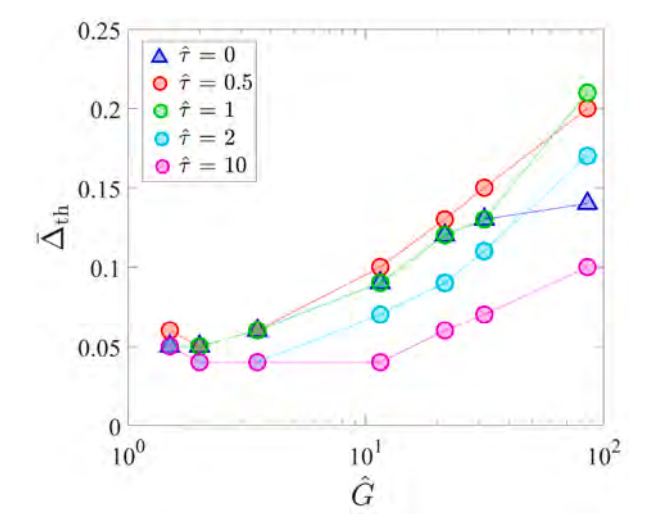


Fig. 5. Dependence of $\bar{\Delta}_{th}$ (Eq. (6)) on relaxation parameters for $\dot{\bar{\epsilon}} = 0.03 \text{ s}^{-1}$.

the interaction between the loading time-scale $(t_L=1/\dot{\epsilon})$ and the bulk relaxation time-scale (τ_k) . Thus, for a material with a given relaxation modulus ratio, a shorter bulk relaxation time-scale tends to hasten the transition from the β_0 -regime to the β_1 -regime. On the other hand, when $\tau_k \approx \infty$ (i.e., $\hat{\tau}=0$) the $\beta_0 \to \beta_1$ transition is solely driven by the shear relaxation time-scale. From the figure, we see that the $\hat{\tau}=0$ case follows the same dependence on \hat{G} as for the equi-relaxing material ($\hat{\tau}=1$) except at $\hat{G}=85.5$ where the value tends to saturate at the level corresponding to $\hat{G}=31.5$. While the reason behind this trend is not yet clear, it suggests that above a certain value the relaxation modulus ratio may not be significant in the transition for $\hat{\tau}=0$.

At $\dot{\varepsilon}=0.3~{\rm s}^{-1}$ (not shown in Fig. 5 for brevity), $\bar{A}_{\rm th}$ is observed only for $\hat{\tau}=10$ at $\hat{G}=31.5$ and 85.5. Moreover it is constant $(\bar{A}_{\rm th}\sim0.45)$ for both materials. For $\dot{\bar{\varepsilon}}=1~{\rm s}^{-1}$, $\bar{A}_{\rm th}$ does not exist and the responses are entirely described by the elasticity governed regime (i.e., β_1). With these characteristics, Fig. 6 collates the dependencies of S_0, S_1, β_0 and β_1 on the material parameters. We use the FMINCON function in MATLAB® to obtain optimal values of these parameters; the R^2 values in the optimization of these parameters are \sim 0.97. For brevity, we show the trends only for $\dot{\bar{\varepsilon}}=0.03~{\rm s}^{-1}$ and later we briefly comment on their counterparts at higher strain rates. Figs. 6(a) and 6(b) respectively show the dependence of S_0 and β_0 on the relaxation parameter ratios. It reveals that the normalized force—displacement relation in the dissipation-governed regime is relatively insensitive to \hat{G} (save for $\hat{\tau}=10$) and is primarily dictated by the relaxation time-scales. Their decrease with increasing $\hat{\tau}$ indicates that, in the dissipation-governed regime, as the bulk relaxation time-scale (τ_k) becomes important relative to the shear relaxation time scale (τ_r) the system requires

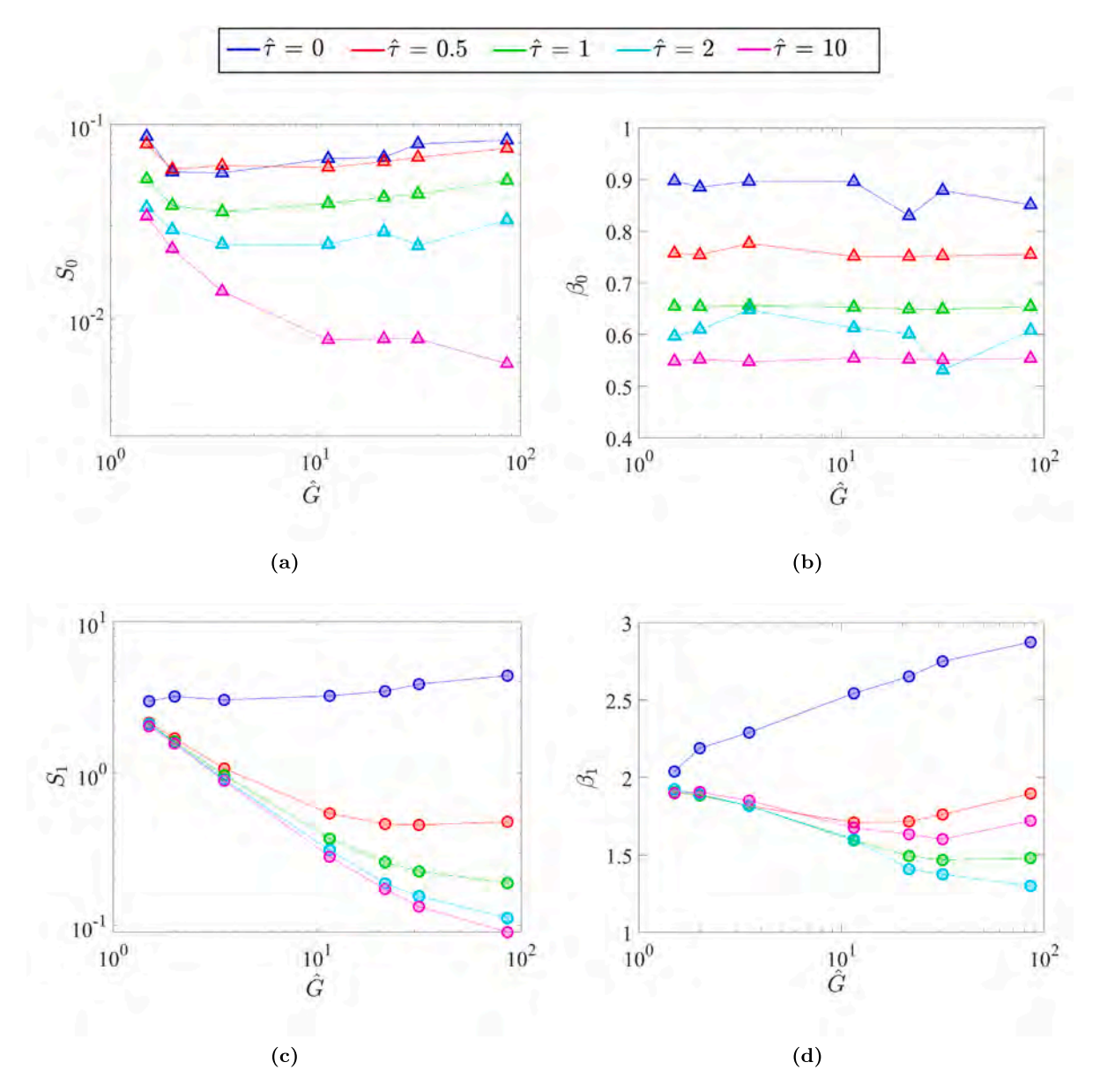


Fig. 6. Dependence of (a) S_0 , (b) β_0 , (c) S_1 and (d) β_1 in Eq. (6) on relaxation parameters at $\dot{\varepsilon} = 0.03 \text{ s}^{-1}$. Similar qualitative trends are seen at $\dot{\varepsilon} = 0.3 \text{ s}^{-1}$ and $\dot{\varepsilon} = 1 \text{ s}^{-1}$.

a lower normalized force $(\bar{\sigma})$ to sustain a given level of compaction (i.e., $\bar{\Delta} \leq \bar{\Delta}_{th}$). Note that this $\bar{\sigma}$ is nearly independent of the relaxation modulus ratio.

On the other hand, in the elasticity-governed regime (Figs. 6(c) and 6(d)) the force–displacement relation is affected by both, \hat{G} and $\hat{\tau}$. When some amount of bulk relaxation is active ($\hat{\tau} > 0$), the general trend is that both S_1 and β_1 decrease with increasing \hat{G} . Given that $\beta_1 > 1$, how much force is required to achieve a desired level of compaction ($\bar{\Delta} > \bar{\Delta}_{th}$) will depend on the net effect of S_1 and β_1 although the general trend appears to be that larger the $\hat{\tau}$ (for a given \hat{G}) lower the normalized force.

Combining these effects from the two regimes, it can be said that the normalized peak force $(\bar{\sigma}_{peak})$ required to achieve complete compaction (i.e., zero porosity) decreases as the bulk relaxation time-scale becomes more and more important relative to the shear relaxation time-scale. For the purely shear relaxing case $(\hat{\tau} = 0)$, the increasing value of β_1 with \hat{G} ascertains the increasingly softer force–displacement relation with increasing relaxation modulus ratio.

At the other end, for $\dot{\epsilon}=1$ s⁻¹ only S_1 and β_1 are relevant; see Fig. B.2 in Appendix B. The trends for S_1 (Fig. B.2(a)) are qualitatively largely similar to their counterparts at $\dot{\epsilon}=0.03$ s⁻¹. On the other hand, β_1 (cf. Fig. B.2(b)) is independent of \hat{G} for $\hat{\tau}=0$ unlike at $\dot{\epsilon}=0.03$ s⁻¹. For $\hat{\tau}>0$, β_1 decreases with increasing \hat{G} and it decreases faster with increasing $\hat{\tau}$.

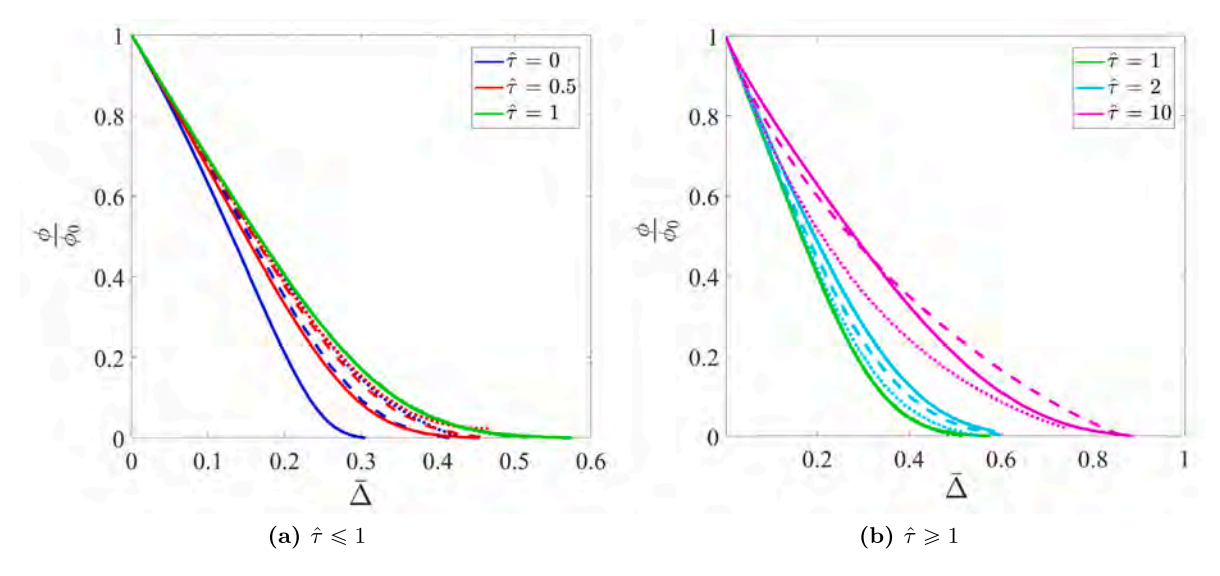


Fig. 7. Rate-dependent porosity evolution from finite element simulations for $\hat{G} = 85.5$. $\dot{\varepsilon} = 0.03 \text{ s}^{-1}$ (----), $\dot{\varepsilon} = 0.3 \text{ s}^{-1}$ (----), and $\dot{\varepsilon} = 1.0 \text{ s}^{-1}$ (·····).

While the scaling exponents indicate a departure from the Hertzian solution ($\beta_{\text{Hertz}} \approx 1$) for a linearly elastic, cylinder-cylinder contact (Nakhatakyan, 2011; Barber, 2018), the power-law dependence (Eq. (6)) is in concert with three-dimensional experiments (e.g., Brodu et al., 2015). Another discriminating feature is the presence of two regimes: one governed by viscous dissipation (β_0) and the other elasticity dominant (β_1). Admittedly, the two regimes cannot be fully isolated as both effects will be present throughout the deformation process. Notwithstanding, some of the salient trends are noteworthy. For relatively elastic materials ($\hat{G} \lesssim 3$), we find $1.75 \lesssim \beta_1 \lesssim 2.4$ over the range of relaxation time-scale ratios. Its weak dependence on the applied strain rate emphasizes a dominantly elastic response of these materials beyond the threshold displacement (\bar{A}_{th}). For increasingly viscoelastic cases ($\hat{G} \gtrsim 3.5$) the range of β_1 with respect to $\hat{\tau}$ is much larger and it increases with increasing \hat{G} (cf. Figs. 6(b) and B.2(b)), which underscores role of viscous effects beyond \bar{A}_{th} .

3.2. Porosity evolution

As the granular assembly is compressed, the interstitial spaces get compacted causing the overall porosity (ϕ) to evolve with time (t). The porosity is defined as (cf. Fig. 2),

$$\phi(t) = 1 - \frac{A_p(t)}{A_c(t)} \tag{7}$$

where $A_c(t) = L_x(t)L_y(t)$ is the current area of the cell and $A_p(t)$ is the current total area of all the particles in the unit cell, i.e. $A_p(t) = \sum_{i=1}^{N_p} \sum_{j=1}^{N} a_j^i(t)$ where $a_j^i(t)$ is the current area of the jth finite element in particle i, N the total number of finite elements in the particle, and N_p the total number of particles in the unit cell.

Fig. 7 reveals the viscoelastic effect on the porosity evolution for $\hat{G}=85.5$. For clarity the results are separated according to the $\hat{\tau}$ regimes. For a fixed $\dot{\bar{\epsilon}}$ (say $\dot{\bar{\epsilon}}=0.03~\text{s}^{-1}$, solid lines), the porosity decreases more slowly with increasing $\hat{\tau}$ values, i.e., as the bulk relaxation time-scale becomes increasingly relevant. To that end, note that in a granular system the applied deformation $(\bar{\Delta})$ is accommodated by two processes — (i) particle deformation and (ii) compaction, i.e., porosity reduction. It suggests that the macroscopic deformation in granular systems with faster bulk relaxation is preferentially accommodated via volume change of the particles compared to porosity reduction. Indeed, referring to Fig. A.1(c), it can be seen that bulk relaxing materials ($\hat{\tau}>1$) exhibit a temporary increase in the compressibility (decrease in the material Poisson's ratio) with time. In comparison, shear relaxing materials ($\hat{\tau}<1$) the applied deformation is preferentially accommodated via porosity reduction as the material resists volume change, indicated by an increase in the Poisson's ratio with time.

This characteristic dependence of the porosity evolution on $\hat{\tau}$ can explain the stiffening effect seen in the force–displacement responses (cf. Figs. 3 and 9(a)). Stiffening occurs when the normalized porosity reaches a certain threshold, which is found to be \sim 0.2. In a shear relaxing granular lattice, this threshold value is reached sooner because porosity evolution is the preferred process of compaction. By contrast, the threshold is reached later in a bulk relaxing lattice as compaction is accommodated preferentially by particle volume change.

With *increasing* $\dot{\epsilon}$, a shear relaxing material with a particular $\hat{\tau} < 1$ exhibits a *slower* decrease in porosity (Fig. 7(a)). By contrast, for a bulk relaxing material ($\hat{\tau} > 1$) the porosity reduction is *faster* with increasing $\dot{\epsilon}$, cf. Fig. 7(b). This may be again understood in terms of the compressibility effects that arise due to the interaction between the shear and bulk relaxation time-scales as well as the relaxation moduli, cf. Fig. A.1(c). Consider a particular level of applied deformation, $\bar{\Delta} = \dot{\epsilon} \times t$. In a bulk relaxing material, the

decrease in Poisson's ratio with increasing loading rate is smaller. Thus, the particles are less compressible at a higher rate than at a lower rate for the same $\bar{\Delta}$. As a result, the applied deformation ($\bar{\Delta}$) must now be accommodated by enhanced porosity reduction. Extending this argument to a shear relaxing material, a higher loading rate causes a smaller increase in the Poisson's ratio for a given $\bar{\Delta}$, which implies a higher compressibility of the particles at a higher strain rate relative to a lower strain rate. As a result, the applied deformation at a higher rate can now be accommodated by enhanced particle compression thereby causing lesser porosity decrease.

These qualitative characteristics persist for other $\hat{G} - \hat{\varepsilon}$ combinations as shown in Fig. B.3 of Appendix B. Combining the results in Fig. 7 with those in Fig. B.3, we see that for a fixed $\hat{\varepsilon}$, higher \hat{G} leads to a faster decrease in porosity for $\hat{\tau} < 1$. In comparison, for $\hat{\tau} > 1$, higher \hat{G} results in a slower decrease in porosity. For $\hat{\tau} = 1$, the trends are independent of $\hat{\varepsilon}$ and \hat{G} .

4. An analytical model for porosity evolution

In discrete granular mechanics, the macroscopic force is related to the average number of contacts per particle ($\langle Z \rangle$), which is empirically related to the porosity (or the packing fraction) (O'hern et al., 2003; Brodu et al., 2015; Vu et al., 2019; Cantor et al., 2020). Hence, it is useful to obtain a relationship between the porosity and applied deformation. Here, we present an analytical model to describe the porosity evolution that is related to macroscopic deformation. The nonlinear and rate-dependent porosity evolution described in Section 3.2 is a result of intricate interaction between the material parameters, contact mechanics, and the rate of loading. We define the total areal strain of particles $\epsilon_p(t)$ and the nominal cell areal strain $\epsilon_c(t)$ as:

$$\epsilon_p(t) = \frac{A_p(t)}{A_p^0} - 1$$
 ; $\epsilon_c(t) = \frac{A_c(t)}{A_c^0} - 1$ (8)

where $A_p^0=A_p(t=0)$ and $A_c^0=A_c(t=0)=L_x^0L_y^0$. In the present work, $L_x^0=L_y^0=d_0$. With $L_x(t)=L_x^0$, $\epsilon_c\equiv\bar{\Delta}$. Noting that at t=0 the initial porosity $\phi_0=1-A_p^0/A_c^0$, we obtain the current porosity from Eq. (7) and Eq. (8) as:

$$\phi(t) = 1 - \frac{(1 - \phi_0)(1 + \epsilon_p(t))}{(1 + \epsilon_c(t))} \tag{9}$$

where $\epsilon_p(t) \leq 0$ and $\epsilon_c(t) \leq 0$ (i.e., compressive). Our finite element calculations (e.g., Fig. B.4) indicate that, over the range of \hat{G} the evolution of ϵ_p is nonlinear with respect to ϵ_c and monotonic with respect to $\dot{\epsilon}$ and $\hat{\tau}$. Based on this, we approximate $\epsilon_p = \alpha(\epsilon_c)^n$, where α and n are fitting parameters. Thus, at time t, Eq. (9) becomes:

$$\phi = 1 - \frac{(1 - \phi_0)[1 + \alpha(\epsilon_c)^n]}{1 + \epsilon_c}$$
(10)

which describes the porosity evolution in terms of the known parameters $\epsilon_c(t)$ and ϕ_0 with two fitting parameters, α and n that account for inter-particle contact interaction and depend on the relaxation parameters as well as the loading rate. Fig. 8 shows the values of α and n calibrated to the finite element results using the FMINCON function in MATLAB® with an $R^2 \sim 0.99$. A full comparison of the results from the analytical model with the finite element calculations over the range of \hat{G} and $\hat{\tau}$ are collated in Fig. B.3 in Appendix B. At a given strain rate, the trends of α and n with respect to \hat{G} (for a given $\hat{\tau}$) are qualitatively the same.

When the viscous effect is governed by shear relaxation ($\hat{\tau} < 1$), α (Figs. 8(a), 8(b), and 8(c)) and n (Figs. 8(d), 8(e), and 8(f)) increase with increasing relaxation modulus ratio (\hat{G}). On the other hand, as bulk relaxation process becomes important ($\hat{\tau} > 1$) this behavior transitions to both, α and n decreasing with increasing \hat{G} . There is a clear demarcation at $\hat{\tau} = 1$ where both, α and n are independent of \hat{G} . Referring to Eq. (10), the trends of α and n indicate that for a given relaxation modulus ratio (\hat{G}) and strain rate (\hat{e}) the deformation needed to achieve a desired level of compaction should increase as bulk relaxation time-scale starts playing a role i.e., with increasing $\hat{\tau}$.

5. Further discussion

The finite element simulations performed here assume a linear viscoelastic constitutive behavior of the particles while considering finite strain effects. A more refined analysis may account for nonlinear viscoelastic rheology, although there is experimental evidence that some polymers may follow a linear viscoelastic behavior at large deformations (e.g., Chen et al., 2020; Commins and Siviour, 2023). Such complications are not considered here with the goal of expressing the basic mechanics in terms of constituent properties. With this caveat, we present an extended discussion of the results from the present calculations.

5.1. The relevance of packing

The salient mechanical characteristics described in the preceding sections highlight the role of constituent material properties in the macroscopic behavior of granular lattices. The role of the granular motif is embedded in these behaviors but the role of multi-particle interaction is not explicitly addressed. Essentially, the questions are: (i) How does granular lattice differ from the response of a single particle? and (ii) What role does lattice arrangement play in the macroscopic behavior? While a full set of calculations is beyond the scope of this work, we present some basic comparisons that offer some insights in to these questions.

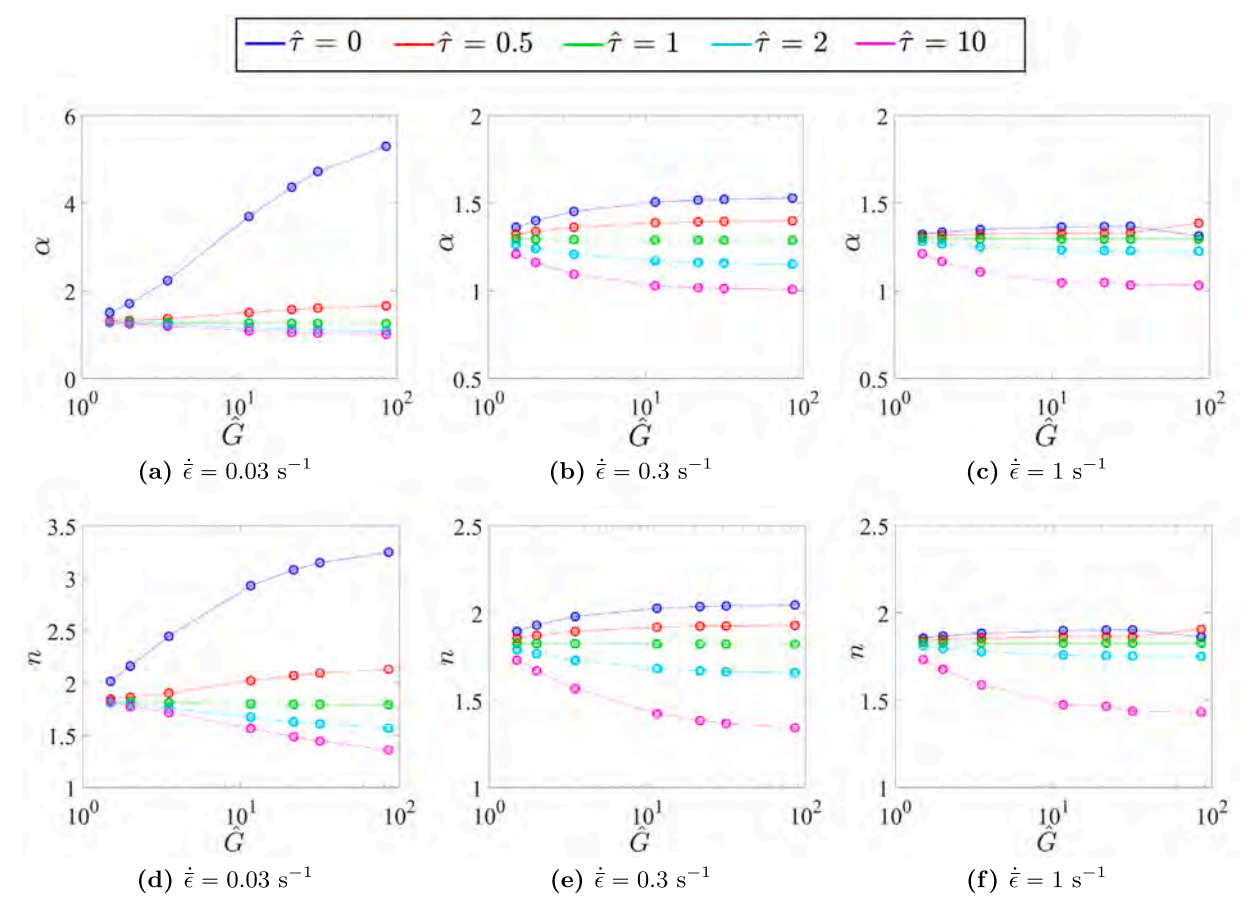


Fig. 8. Dependence of parameters α and n on \hat{G} for different $\hat{\tau}$ (colors) values at (a, d) $\hat{\epsilon} = 0.03 \text{ s}^{-1}$, (b, e) $\hat{\epsilon} = 0.3 \text{ s}^{-1}$, and (c, f) $\hat{\epsilon} = 1 \text{ s}^{-1}$.

5.1.1. Granular lattice versus single particle

The role of granular packing is illustrated in Fig. 9 by comparing the behaviors of the square granular lattice and single particle under compression. Results are shown for two cases of $\hat{\tau}$ ratios keeping the relaxation modulus ratio the same ($\hat{G} = 85.5$). In Fig. 9(a), two aspects become clear. First, for a shear relaxing material (e.g., $\hat{\tau} = 0$) the confinement effect in the granular packing produces a force–displacement response that is significantly stiffer than the single particle made of same material. That is not the case for a bulk relaxing material (e.g., $\hat{\tau} = 2$) which shows a negligible confinement effect. Second, the confinement effect significantly amplifies the difference in the responses of shear relaxing and bulk relaxing lattices (solid lines in Fig. 9(a)), which in the case of single particle cases is negligible (dashed lines in Fig. 9(a)).

The energy ratio (\mathcal{E}) in Fig. 9(b) reveals that the elastic effects tend to become important in both shear and bulk granular lattices at relatively moderate deformation levels. In comparison, the response of single particles is dominated by viscous effects up to much larger deformation levels. Further, the \mathcal{E} ratio for a single particle does not exhibit the non-monotonic behavior seen in the granular assemblies suggesting that their force–displacement responses can be described by a single power law.

In sum, the characteristics described in the preceding sections are peculiar to granular packings.

5.1.2. Type of packing

To discern the role of lattice architecture, a limited set of calculations (for $\hat{G} = 85.5$ and $\hat{\tau} \in \{0,1,2\}$) are performed for hexagonally-packed granular lattices. As illustrated in Fig. 10, a hexagonal granular lattices exhibit qualitatively similar responses as square granular lattice; quantitatively, for a given set of material parameters the hexagonal arrangement exhibits a stiffer mechanical behavior and faster porosity evolution relative to a square packing. With respect to $\hat{\tau}$, the normalized force and porosity trends are consistent with those in the square granular lattice. As such, we expect the main observations made pertaining to square granular lattices to remain valid.

5.2. Force versus packing fraction

In Sections 4 and 3.1, the trends for the force exponents (β_0 and β_1) and the porosity exponent (n) show somewhat similar dependencies on the material parameters. This motivates insights into force-packing fraction ($\bar{\sigma} - \psi$) relations, which are often

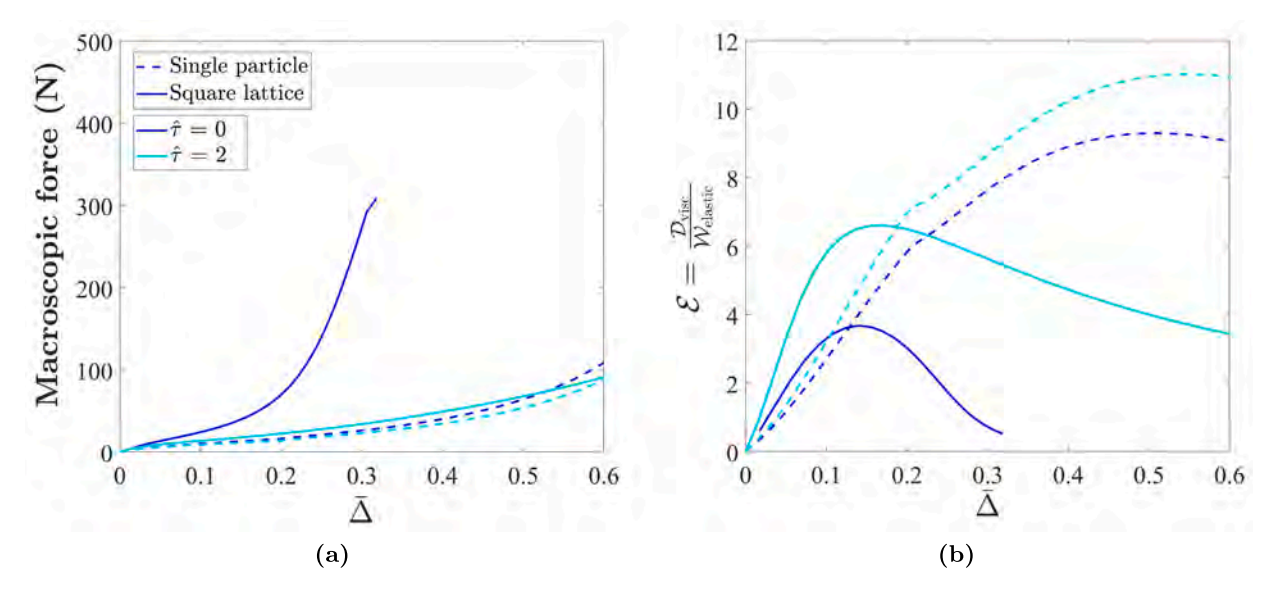


Fig. 9. Comparison of (a) macroscopic force–displacement relations and (b) corresponding evolution of the ratio (\mathcal{E}) for single particle (dashed) and square granular lattice (solid). Results are illustrated for $\hat{G} = 85.5$ at $\dot{\epsilon} = 0.03$ s⁻¹.

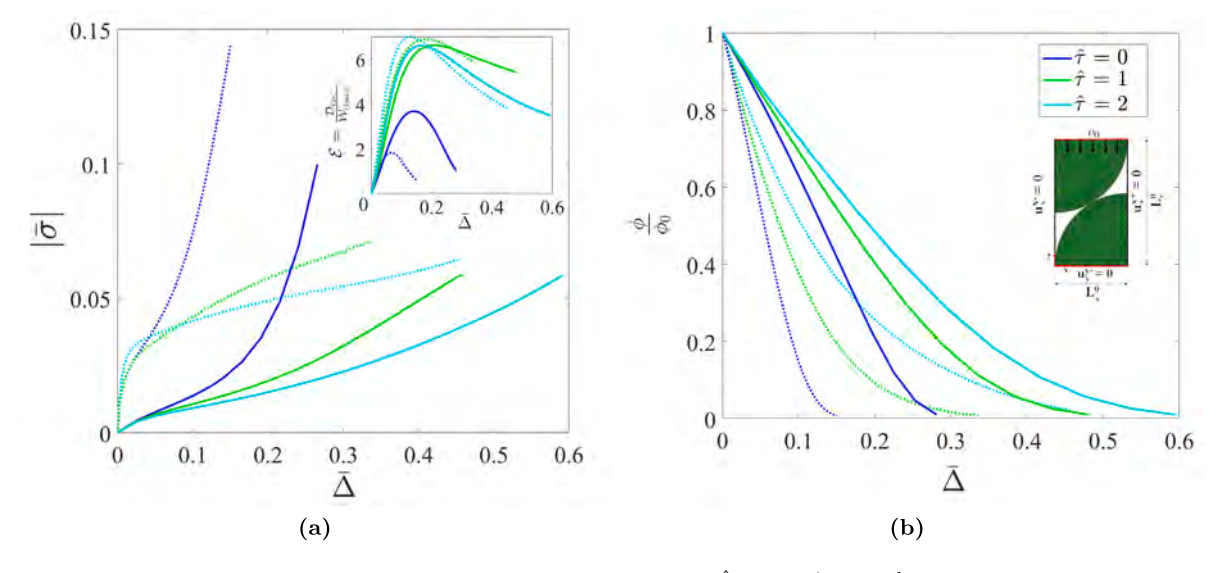


Fig. 10. Illustrative behaviors of hexagonal (\cdots) and square (\longrightarrow) granular lattices for $\hat{G}=85.5$ at $\hat{\epsilon}=0.03$ s⁻¹. Panel (a) normalized force-displacement ($|\bar{\sigma}|-\bar{\Delta}$) and (b) normalized porosity-displacement ($\phi/\phi_0-\bar{\Delta}$). Inset in Panel (a) shows the evolution of the energy ratio (\mathcal{E}). Inset in Panel (b) shows the hexagonal unit cell.

of interest in granular physics (e.g., Cantor et al., 2020). For instance, recent rate-independent DEM simulations of compressible neo-Hookean assemblies (Vu et al., 2021) reveal that while the force-displacement responses are sensitive to Poisson's ratio (ν), the normalized force-packing fraction ($\bar{\sigma} - \psi$) relation is insensitive to it over a wide range of ν . Fig. 11 illustrates the $\bar{\sigma} - \psi$ relation for $\dot{\bar{e}} = 0.03 \text{ s}^{-1}$ where $\psi = (1 - \phi)$. For comparison, trends from the model (combining Eq. (6) and Eq. (10)) are included and they corroborate with the finite element results (symbols). The qualitative trends are consistent with recent two-dimensional DEM simulations (Cantor et al., 2020; Vu et al., 2021) showing an initial soft response culminating into a rapid stiffening as $\psi \to 1$. Recall that for a given relaxation modulus ratio (\hat{G}), the Poisson's ratio (ν) depends on $\hat{\tau}$, cf. Eq. (A.1). Thus, any dependence on $\hat{\tau}$ can be effectively seen as a dependence on ν . As seen from Fig. 11, the value of the relaxation modulus ratio (\hat{G}) dictates whether the $\bar{\sigma} - \psi$ relation is sensitive to ν . For $\hat{G} \lesssim 11.5$ (illustrated in Fig. 11(a)), the responses are insensitive to $\hat{\tau}$ similar to Vu et al. (2021). By contrast, for $\hat{G} \gtrsim 21.5$ (Fig. 11(b)) the responses effectively depend on ν via $\hat{\tau}$.

Recall that $\bar{\sigma} - \bar{\Delta}$ (Fig. 3) and $\phi - \bar{\Delta}$ (Fig. 7) responses begin to show a dependence on $\hat{\tau}$ at relatively modest levels of \hat{G} . Against that backdrop, it is interesting that the $\bar{\sigma} - \psi$ responses show no or mild sensitivity to $\hat{\tau}$. It thus appears that while the constituent

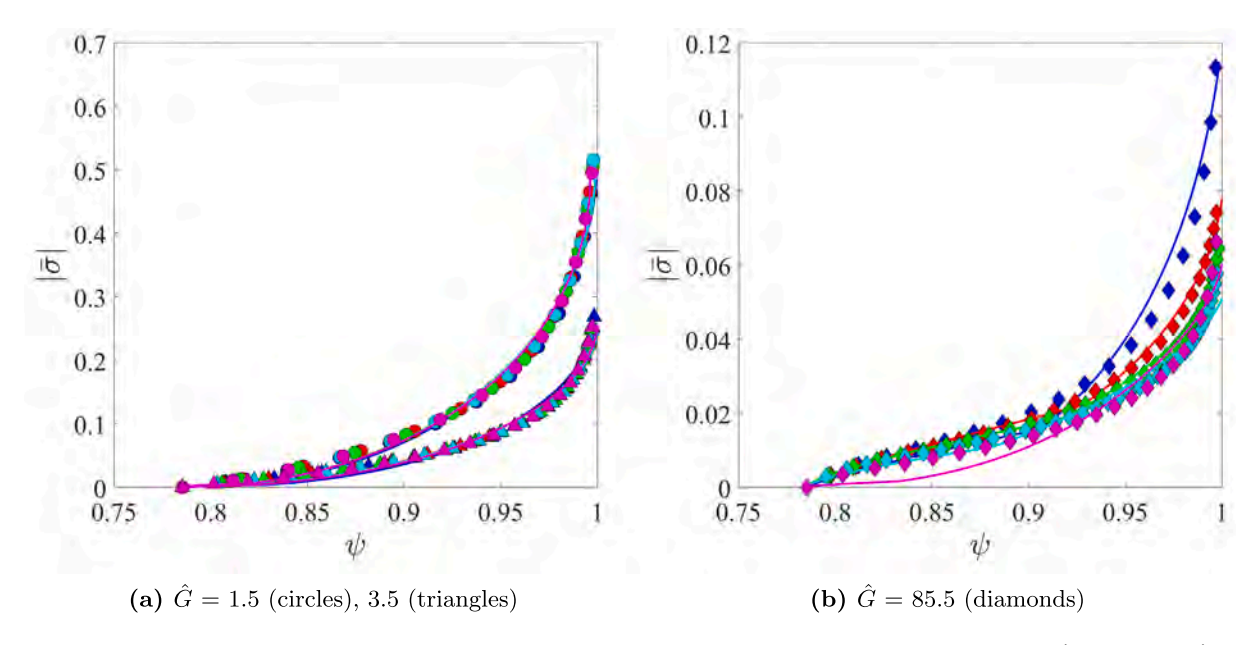


Fig. 11. Finite element (symbols) and model (lines) results of normalized force versus packing fraction $(\bar{\sigma}-\psi)$ at $\dot{\bar{\epsilon}}=0.03~\text{s}^{-1}$ for (a) $\hat{G}=1.5$ (circles), $\hat{G}=3.5$ (triangles), (b) $\hat{G}=85.5$. $\hat{\tau}=0$ (blue), $\hat{\tau}=0.5$ (red), $\hat{\tau}=1$ (green), $\hat{\tau}=2$ (cyan), $\hat{\tau}=10$ (magenta).

parameters $(\hat{G} \text{ and } \hat{\tau})$ may strongly influence the macroscopic force and porosity evolution individually, their net effect viewed as force-packing fraction relation may be much tempered or even negligible. It is possible that for higher \hat{G} ratios the effect of $\hat{\tau}$ may be more discernible. Notwithstanding, when the response does depends on ν (e.g., Fig. 11(b)) it is the stiffest for the shear-relaxing material $(\hat{\tau}=0)$ and weakens as the bulk relaxation time-scale becomes important $(\hat{\tau}>0)$ to the extent that for $\hat{\tau}\gtrsim 1$ they are nearly identical.

We note in passing that for 2D incompressible neo-Hookean particle assemblies, Vu et al. (2019) found the packing fraction to be nearly linearly proportional to the applied compressive strain. By way of comparison, Eq. (7) and Fig. B.4 indicate a non-linear relation over the range of material and loading parameters examined but particularly in the incompressibility limit, which corresponds to $\hat{\tau} = 0$ where $v(t) \to 0.5$ as a function of t, cf. Eq. (A.1) and Fig. A.1(c).

5.3. Critical values

Eq. (10) offers a way to predict critical quantities corresponding to complete compaction, which yields:

$$\epsilon_c^{\text{cr}} + \phi_0 - \alpha (1 - \phi_0) (\epsilon_c^{\text{cr}})^n = 0$$
 (11)

where $\epsilon_c^{\rm cr}$ is the critical strain at $\phi=0$. Eq. (11) is solved numerically for $\epsilon_c^{\rm cr}$ in MATLAB®. From that, we calculate the critical time corresponding to $\phi=0$ as $t^{\rm cr}=\epsilon_c^{\rm cr}\lambda_0/v_0$ where λ_0 is the average distance between the particle centers, which in the present case is d_0 . Fig. 12(a) shows a good comparison between the critical time from the simulations ($t_S^{\rm cr}$) and $t_A^{\rm cr}$ based on Eq. (11). As indicated in Section 4, for a given \hat{G} and $\hat{\epsilon}$, increasing $\hat{\tau}$ increases the time required to achieve full packing. As illustrated in Fig. 12(b), for $\hat{\epsilon}=0.03$ s⁻¹ the magnitudes of the peak normalized force ($|\bar{\sigma}_{peak}|$) corresponding to $t^{\rm cr}$ also compare well. Note that in Fig. 12(b), for a given \hat{G} the peak normalized force decreases with increasing $\hat{\tau}$, albeit mildly consistent with the discussion with reference to Fig. 6.

5.4. Recovery

Finally, we discuss porosity recovery upon unloading. For brevity, we focus on the results for $\hat{c}=0.03$ s⁻¹. Fig. 13 shows the trends for materials with $\hat{G} \in \{1.5, 85.5\}$ and $\hat{\tau} \in \{0, 1, 10\}$. For $\hat{G}=1.5$, the recovery curve closely follows the compaction curve for $\hat{\tau}=0$ (Fig. 13(a)) but the two deviate measurably for $\hat{\tau}=1$ (Fig. 13(b)) and $\hat{\tau}=10$ (Fig. 13(c)). This underscores the importance of the bulk relaxation process, which is controlled by $\hat{\tau}$ (given that $\hat{K}=\hat{G}$). When bulk relaxation is slow the shear-driven viscoelasticity is not of primary consequence insofar as the recovery is concerned. In contrast, when the bulk relaxation is equal to or faster than the shear relaxation, the recovery process is affected.

Notice that in all three cases at $\hat{G} = 1.5$ a substantial recovery (\sim 60–80%) is elastic (red portion). Interestingly, upon transition from elastic recovery (marked by \times) the viscoelastic recovery (green portion) process for $\hat{\tau} = 10$ shows a *slow-then-fast* behavior (note the stagnation) whereas $\hat{\tau} = 1$ shows a *fast-then-slow* behavior.

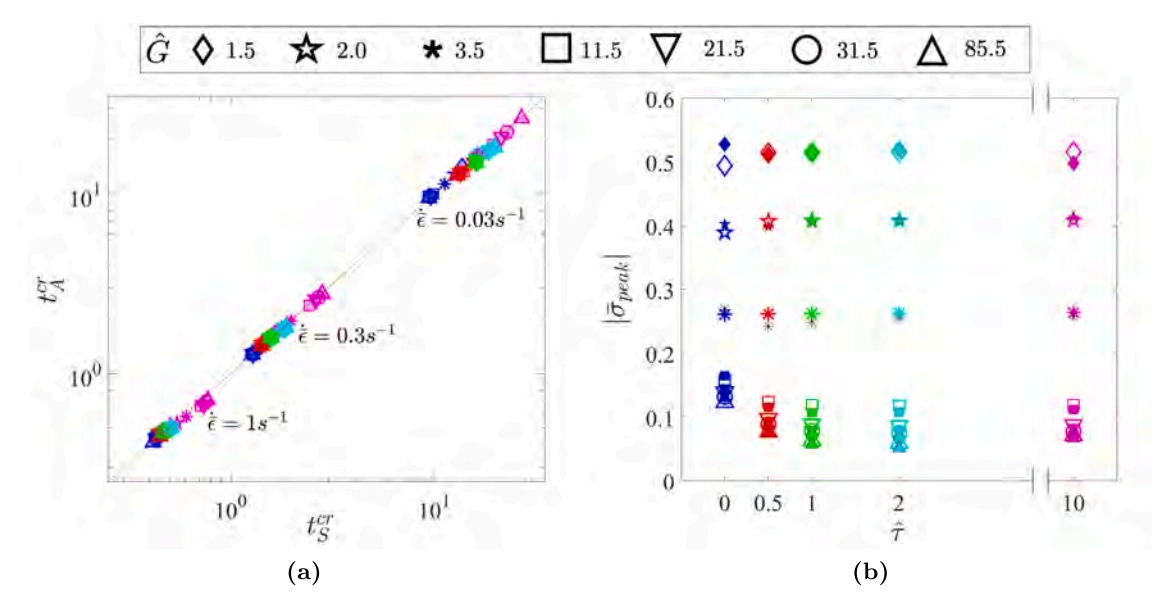


Fig. 12. Comparison between the finite element and model predictions for (a) critical time at $\phi=0$ ($\hat{\tau}=0$ (blue), $\hat{\tau}=0.5$ (red), $\hat{\tau}=1$ (green), $\hat{\tau}=2$ (cyan), $\hat{\tau}=10$ (magenta)), and (b) peak normalized stress (at $\phi=0$) for $\dot{\hat{\epsilon}}=0.03$ s⁻¹; open symbols are finite element results and filled symbols are model results; for $\hat{G}=3.5(*)$, model results are shown by black *.

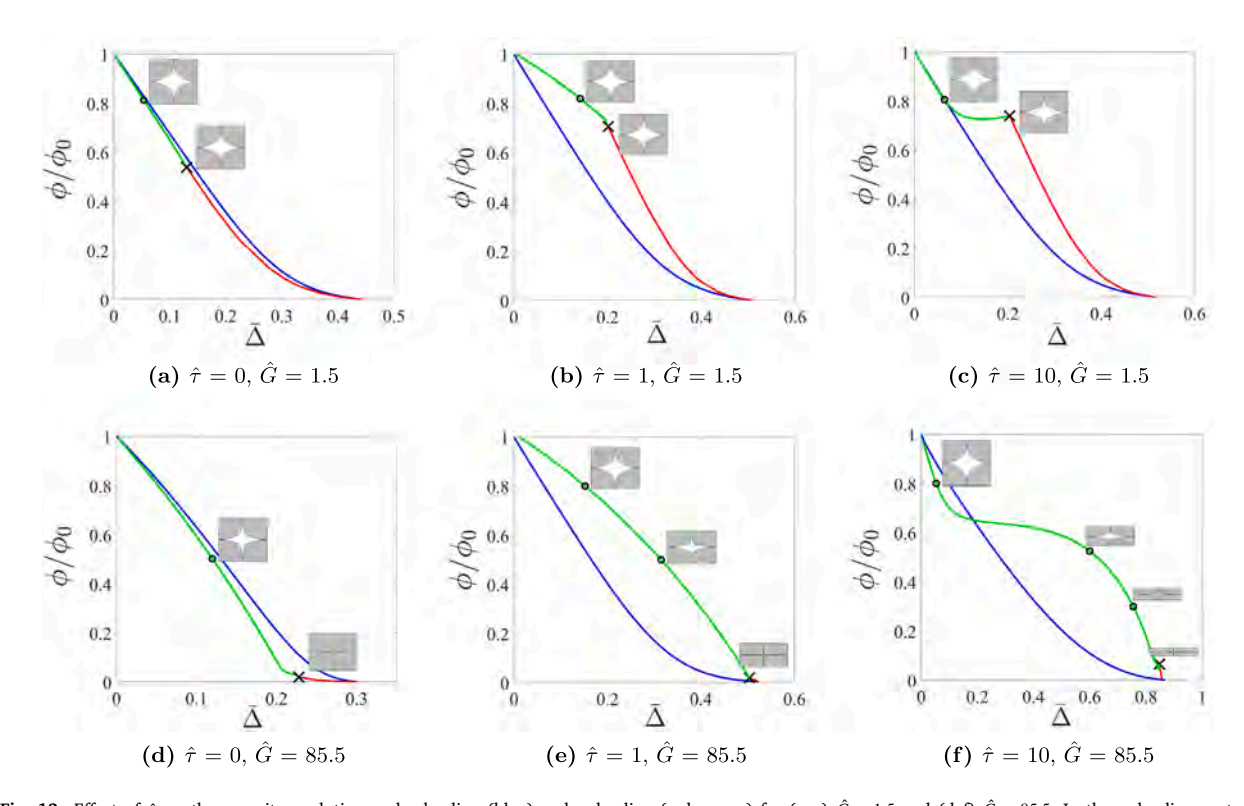


Fig. 13. Effect of \hat{r} on the porosity evolution under loading (blue) and unloading (red, green) for (a–c) $\hat{G}=1.5$ and (d–f) $\hat{G}=85.5$. In the unloading parts, the red portion indicates instantaneous elastic rebound and the green portion corresponds to the viscoelastic recovery. The transition from elastic to viscoelastic recovery is marked by ×. Insets in each subfigure show deformed shapes during recovery at particular $\bar{\Delta}$.

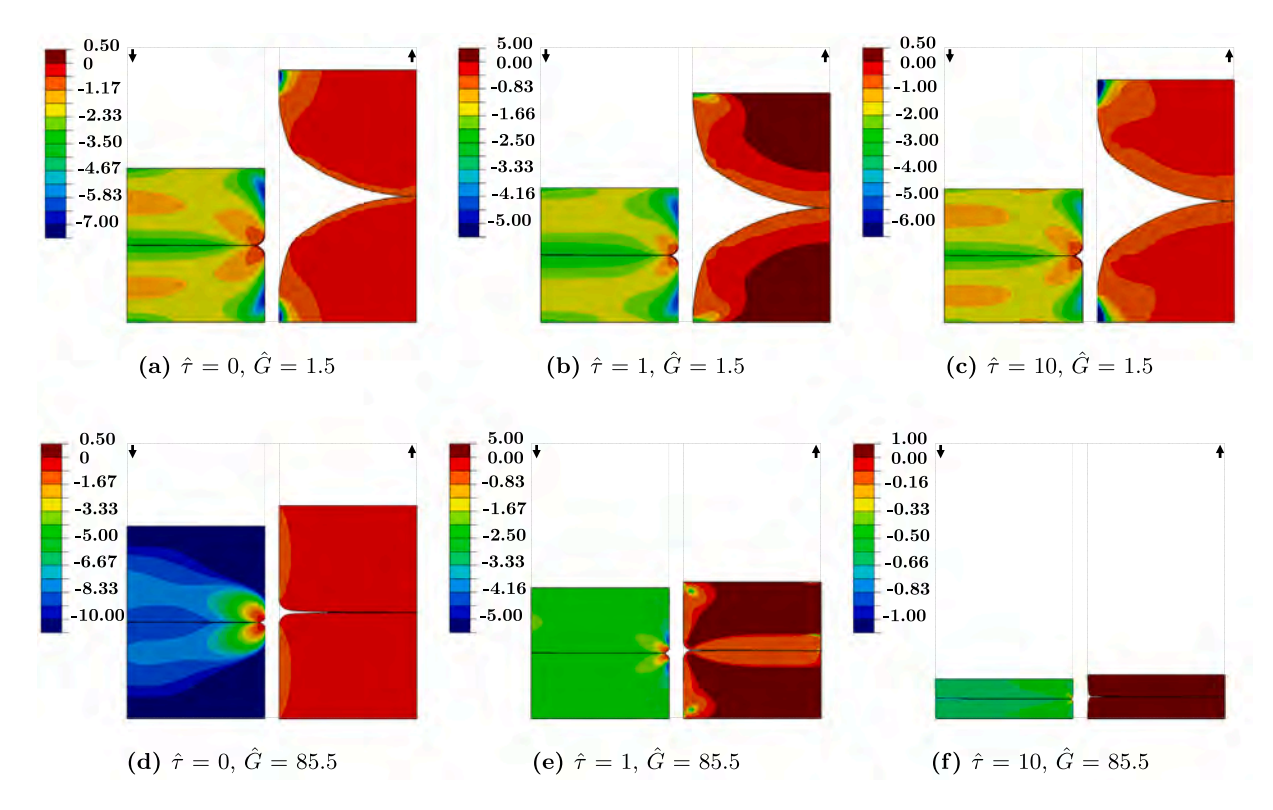


Fig. 14. Stress triaxiality distributions for the cases shown in Fig. 13. In panels (a-f), only half unit cells are shown for clarity. In each panel, the left half shows the loaded state (\downarrow) at $\phi/\phi_0 \sim 0.01$ and the right half shows the recovery state (\uparrow) at e-ve transition (\times in Fig. 13). Positive values indicate tension.

As expected, for $\hat{G}=85.5$ the recovery process is dominated by viscoelasticity. Yet, the effect of $\hat{\tau}$ on the recovery is seen, cf. Figs. 13(d)–13(f). The recovery curve is faster for $\hat{\tau}=0$ compared to its counterparts for $\hat{\tau}=1$ and 10. Notably, for $\hat{\tau}=0$ there is no change in the porosity during the elastic unloading and the entire recovery is viscoelastic. While the elastic recovery of the porosity is negligible for $\hat{\tau}=1$ and 10, the elastic strains are also negligible in the latter two cases compared to $\hat{\tau}=0$. Moreover, the viscoelastic recovery at $\hat{\tau}=10$ shows a rather peculiar sigmoidal-type behavior denoting a fast–slow–fast characteristic, which is not seen for $\hat{\tau}=1$. The insets in each sub-figure depict the deformed shapes of the particles that dictate the porosity recovery. With increasing $\hat{\tau}$ the pore shape becomes increasingly anisotropic during recovery. This is most clearly seen for $\hat{G}=85.5$ (Figs. 13(d)–13(f)) where the viscoelastic recovery process renders a symmetry-breaking pore shape evolution with increasing $\hat{\tau}$. For instance at $\phi/\phi_0 \sim 0.5$, Figs. 13(d)–13(f) reveal that the pore shape is more or less isotropic at $\hat{\tau}=0$ unlike a highly flattened pore shape at $\hat{\tau}=10$.

With the stress relaxation that depends on both $\hat{G}(=\hat{K})$ and $\hat{\tau}$, it is interesting to analyze how these material parameters influence the stress distributions within the unit cell. In the present context, we consider the stress triaxiality ratio as a scalar measure to understand the role of material parameters in stress relaxation: $\mathcal{T}(x,t) = p(x)/\sigma_{\rm eq}(x)$ where p(x) is the hydrostatic stress and $\sigma_{\rm eq}$ is the von Mises equivalent stress at point x. Fig. 14 shows the distributions of $\mathcal{T}(x)$ for the cases shown in Fig. 13. In each sub-figure, the left half shows the state in the loading phase at $\phi/\phi_0 = 0.01$ (close to full void closure) while the right half shows the state in the unloading phase corresponding to the transition from elastic to viscoelastic (e-ve transition) recovery process (x in Fig. 13). In the loading phase (left portions of each sub-figure) all cases exhibit compressive (negative) triaxiality ratios in the particle bulk, which is expected. Tensile (positive) triaxiality is seen at the particle surfaces that are not yet in contact but it rapidly drops and becomes compressive as contact occurs. For $\hat{\tau} = 0$, very high compressive values ($|\mathcal{T}| \sim 10$) occur for $\hat{G} = 85.5$ (Fig. 14(d)) because σ_{eq} relaxes much more compared to σ_h . In comparison, for $\hat{G} = 1.5$ with $\hat{\tau} = 0$ shows compressive triaxiality levels that are nearly an order of magnitude smaller (Fig. 14(a)). For $\hat{G} = 1.5$, the compressive triaxiality values are similar for the three $\hat{\tau}$ values. In comparison, for $\hat{G} = 85.5$, the peak compressive triaxiality magnitudes strongly depend on $\hat{\tau}$ with $\hat{\tau} = 10$ showing the lowest values, which is expected because the hydrostatic stress relaxes much faster than the deviatoric stress. Another interesting feature is the heterogeneity of \mathcal{T} at contact surfaces, which is preferentially seen along the y-direction contact for $\hat{G} = 1.5$. Similar heterogeneity is also seen along x-direction for $\hat{\tau} = 0$, $\hat{G} = 85.5$. Although not considered in this work, such heterogeneity in the contact stresses may have implications in inter-particle interactions and interfacial instabilities. An interesting aspect in the unloading phase is the prevalence of hydrostatic tensile stress at the *e-ve transition* in the particles for $\hat{\tau} \gtrsim 1$. In materials with $\hat{\tau} = 1$, high levels of tensile hydrostatic stresses exists in the inner core of the particles while the interfaces experience a compressive hydrostatic stress. Interestingly, for

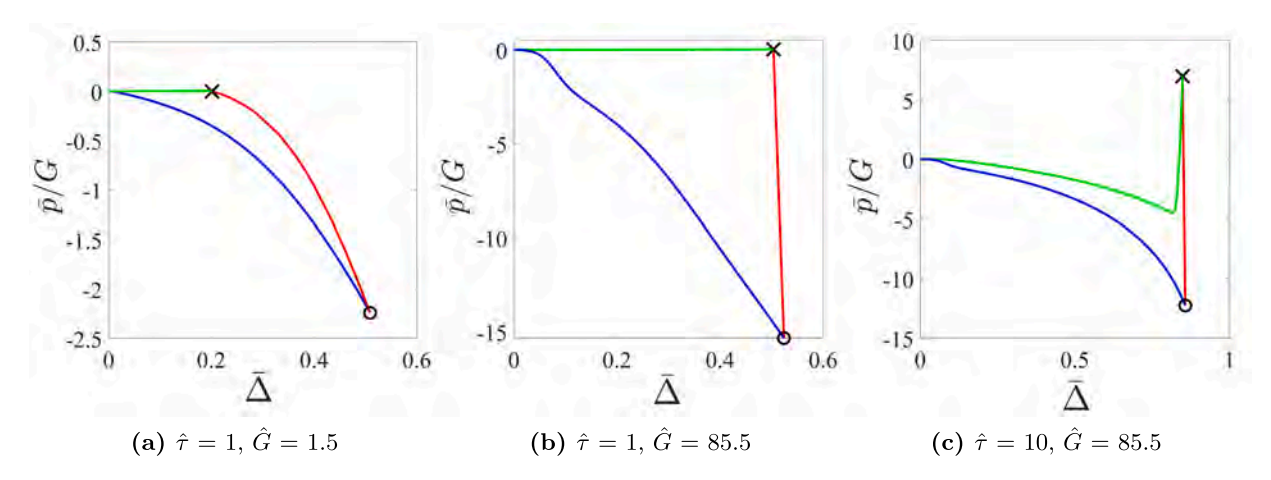


Fig. 15. Evolution of normalized hydrostatic stress ($\bar{p}(t)/G(t)$) under loading (blue) and unloading (red, green) for specific cases of positive triaxiality in Fig. 14. In the unloading parts, the red portion indicates instantaneous elastic rebound and the green portion corresponds to the viscoelastic recovery. The transition from loading to unloading is marked by \bigcirc and elastic to viscoelastic recovery by \times .

 $\hat{G} = 1.5$ and $\hat{\tau} = 10$, the triaxiality is negative while at the same $\hat{\tau}$, it is positive for $\hat{G} = 85.5$. Such high triaxiality levels could cause cavitation within the particles that can lead to damage and ultimate failure.

Fig. 15 shows the volume-averaged hydrostatic stress (\bar{p}) normalized by the current shear relaxation modulus (G) for the three cases in Fig. 14 that show evidence of tensile triaxiality in the unloading phase. While the average tensile pressure is small for $\hat{\tau}=0$ (Fig. 15(a)) and $\hat{\tau}=1$ (Fig. 15(b)), for $\hat{\tau}=10$ (Fig. 15(c)) the value reaches remarkably high levels, albeit for a short period of deformation.⁴ In Fig. 15(c), \bar{p}/G rapidly changes from ~ -13 to $\sim +7.5$ between the start of unloading (marked by \bigcirc) and the start of *e-ve* transition (marked by \times). As viscoelastic recovery process kicks in, \bar{p}/G again rapidly drops to a negative value before gradually reaching zero. We note that in incompressible hyperelastic solids, cavitation is predicted at a theoretical critical value (\bar{p}/G)_{cr} = 2.5 (Gent and Lindley, 1959; Ball, 1982). In compressible neo-Hookean solids, the critical value can be much smaller (Lopez-Pamies, 2009; Cohen and Durban, 2010; Zheng and Cai, 2020). The implications of such *short-lived* but high tensile pressure transient in viscoelastic assemblies are beyond the scope of this paper, but may perhaps be relevant in many situations (e.g., Cohen, 1960; Oberth and Bruenner, 1965; Eom et al., 2001; Huebsch et al., 2015; Lefèvre et al., 2015; Lin et al., 2017; Guo et al., 2020; Barney et al., 2020; Tang et al., 2022).

6. Summary

We perform extensive finite element based DEM simulations of granular lattices modeled using equi-sized cylindrical particles under uniaxial compression. The square lattice architecture is simple but captures essential mechanical features exhibited by nominally mono-disperse granular packings. This simplicity of the model enables studying the role of constituent parameters in their rate-dependent macroscopic behaviors. The salient outcomes peculiar to these granular lattices are as follows:

- 1. The force–displacement behavior exhibits two regimes one governed by viscous dissipation and the other by elastic energy, which arise from the granular confinement effect. There exists a critical deformation state at which the response transitions from being governed by viscous dissipation to that governed by stored elastic energy.
- 2. If the loading time-scale $(t_l = 1/\hat{e})$ is much longer than the shear (τ_g) and bulk (τ_k) relaxation time-scales, both regimes exist. For much shorter loading time-scales only the elasticity governed regime prevails. In both scenarios, the relaxation modulus ratio (i.e., \hat{G}) has a negligible effect. By contrast, \hat{G} plays a role when the loading and relaxation time-scales are comparable. For a given relaxation time-scale ratio $(\hat{\tau})$, there is a critical \hat{G} above which both regimes may exist.
- 3. For a fixed loading rate, the normalized peak force (corresponding to complete compaction) increases as the shear relaxation time-scale becomes more important relative to the bulk relaxation time-scale, and the effect is amplified with increasing \hat{G} .
- 4. The corresponding porosity evolution is also rate-dependent. For a fixed loading rate and relaxation time-scale ratio, a higher \hat{G} leads to faster porosity reduction in shear relaxing materials. The trends are reversed in bulk relaxing materials. For a fixed loading rate and \hat{G} , the porosity reduction rate increases with decreasing relaxation time-scale ratio.

⁴ For the same material parameters, the loading-unloading response of a single particle does not exhibit this behavior.

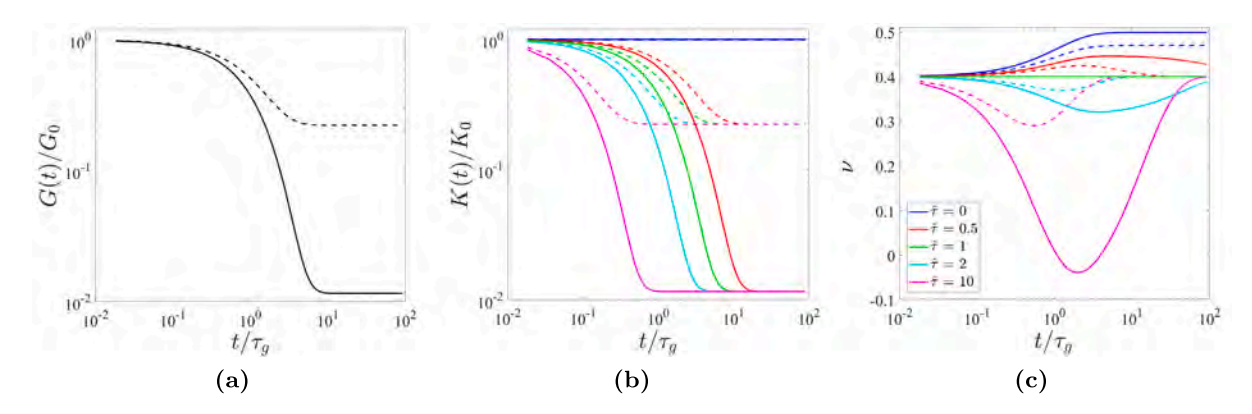


Fig. A.1. Evolution of (a) normalized shear relaxation modulus $(G(t)/G_0)$, (b) Normalized relaxation modulus $(K(t)/K_0)$, and (c) Poisson's ratio (v). Dashed lines: $\hat{G} = \hat{K} = 3.5$: solid lines: $\hat{G} = \hat{K} = 85.5$.

- 5. For a given \hat{G} , although the porosity and force characteristics show a dependence on the relaxation time-scale ratio, the apparent effect in terms of the normalized force-packing fraction relation may be much tempered. Analytical expressions describing their evolution with deformation indicate that their exponents exhibit strong but similar dependencies on the viscoelastic parameters. By consequence, the viscoelastic parameters show a relatively mild effect in the normalized force-packing fraction relation.
- 6. Viscoelastic effects influence porosity recovery during unloading. For certain combinations of relaxation parameters, the pore shape during recovery may become temporarily anisotropic, which affects the rate of recovery. In such scenarios, high tensile pressures may prevail during the transition from elastic to viscoelastic recovery processes.

CRediT authorship contribution statement

Srinivas Selvaraju: Writing – review & editing, Writing – original draft, Software, Methodology, Investigation, Formal analysis. **Shailendra P. Joshi:** Writing – review & editing, Writing – original draft, Supervision, Methodology, Investigation, Funding acquisition, Formal analysis, Conceptualization. **Nikhil Karanjgaokar:** Writing – review & editing, Writing – original draft, Methodology, Investigation, Formal analysis, Conceptualization.

Declaration of competing interest

The authors declare that they have no known competing financial interests or personal relationships that could have appeared to influence the work reported in this paper.

Data availability

No data was used for the research described in the article.

Acknowledgments

SPJ wishes Professor Huajian Gao on his 60th birthday. The authors are thankful to both the reviewers for their constructive comments, which helped improve the manuscript. SPJ and SS acknowledge funding support from the National Science Foundation Mechanics of Materials and Structures Program (NSF-MOMS), United States through CAREER award CMMI #2042498 (Program Director: Dr. Siddiq Qidwai). NK would like to express their gratitude to the NSF-MOMS program, United States for the funding support through the NSF CAREER award #1845200. SPJ and SS acknowledge the use of the Carya cluster and the advanced support from the Research Computing Data Core at the University of Houston, United States to carry out the research presented here.

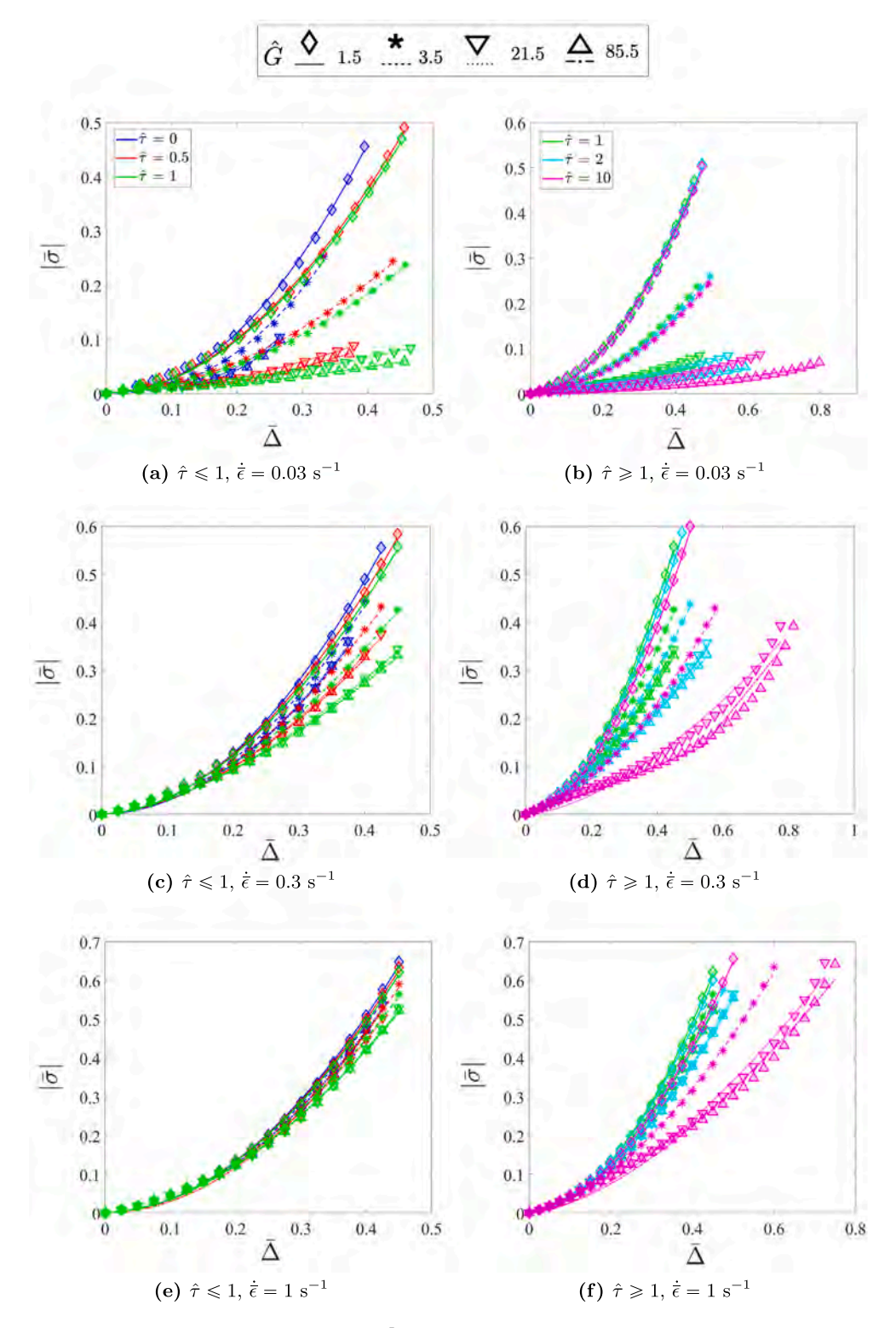


Fig. B.1. Rate-dependent normalized force–displacement $(\bar{\sigma} - \bar{\Delta})$ responses from finite element calculations (symbols) and model (Eq. (6), lines).

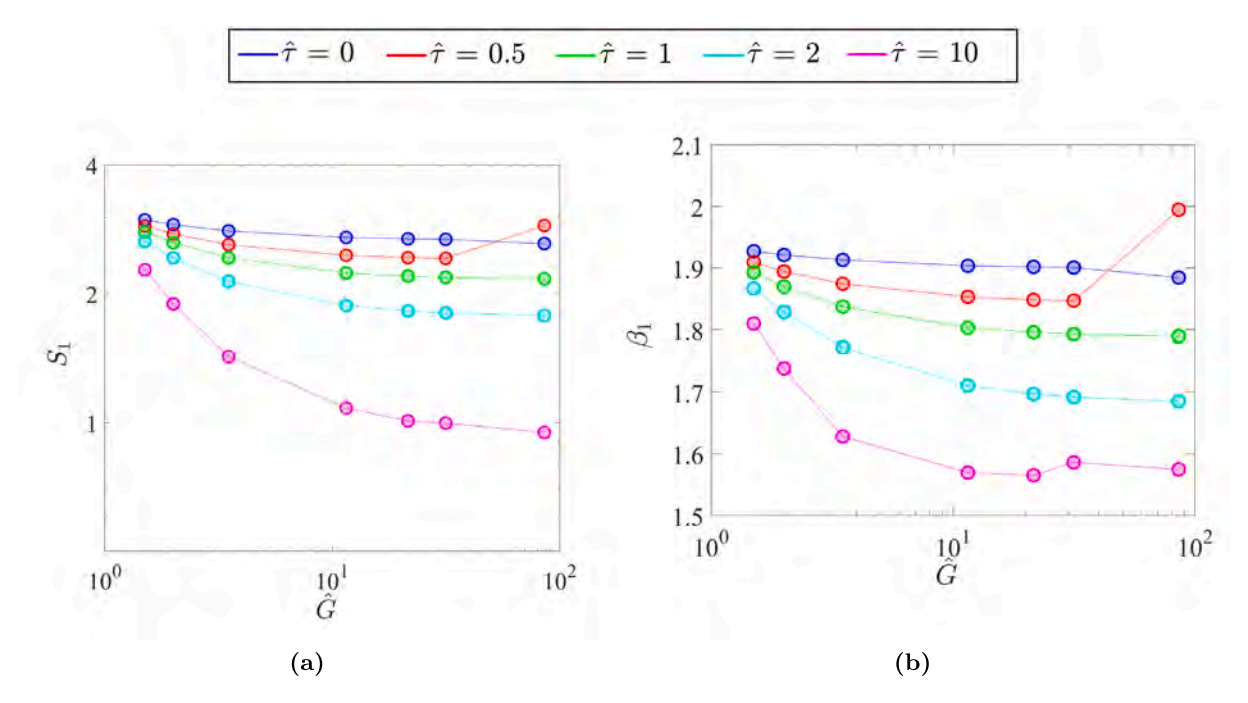


Fig. B.2. Dependence of (a) S_1 and (b) β_1 in Eq. (6) on relaxation parameters at $\dot{\epsilon} = 1 \text{ s}^{-1}$.

Appendix A. Evolution of relaxation parameters with respect to time

Fig. A.1 illustrates the evolution of the relaxation moduli (Figs. A.1(a) and A.1(b)) as a function of the normalized time. Given that $\tau_g = \text{constant}$, the shear relaxation spectra (for a given \hat{G}) are identical for all $\hat{\tau}$ ratios. On the other hand, the bulk relaxation spectra (for a given \hat{K}) depend on $\hat{\tau}$. Although we set $\hat{K} = \hat{G}$, the actual relaxation moduli values at a given time t depend on $\hat{\tau}$ and \hat{c} . Thus, at a given \hat{c} , a material with $\hat{\tau} < 1$ will show higher shear relaxation than the bulk relaxation and vice-versa for a material with $\hat{\tau} > 1$. The resulting Poisson's ratio, v(t) can be obtained analytically as (Fig. A.1(c)):

$$v(s) = \frac{\hat{K}s\tau_g[3\hat{G}K_0(1+s\tau_g) - 2G_0(1+\hat{G}s\tau_g)] + \hat{\tau}[3\hat{G}K_0(1+s\tau_g) - 2\hat{K}(G_0+\hat{G}G_0s\tau_g)]}{2s[\hat{K}s\tau_g[G_0+3\hat{G}K_0+\hat{G}(G_0+3K_0)s\tau_g] + \hat{\tau}[3\hat{G}K_0(1+s\tau_g) + \hat{K}(G_0+\hat{G}G_0s\tau_g)]]}$$
(A.1)

where s is the Laplace variable. Fig. A.1(c) shows that v increases from its instantaneous value toward incompressibility limit for $\hat{\tau} \to 0$; for $\hat{\tau} > 1$, it decreases initially and then increases to reach instantaneous value at sufficiently long time-scales. The amount of decrease depends on \hat{G} and \hat{K} . These trends corroborate with experimental reports on Poisson's ratio measurements (Grassia et al., 2010).

Appendix B. Rate-dependent responses for different relaxation parameters

Fig. B.1 shows the normalized force $(\bar{\sigma})$ versus normalized displacement $\bar{\Delta}$ responses at three $\dot{\bar{c}}$ values. For clarity, the results are shown for $\hat{G} \in \{1.5, 3.5, 21.5, 85.5\}$. Note that the responses terminate at $\phi/\phi_0 = 0$. As seen here, at a given $\dot{\bar{c}}$ the stiffest response for a particular \hat{G} occurs for $\hat{\tau} = 0$ and the softest response occurs for $\hat{\tau} = 10$.

Further, the stiffest (corresponding to $\hat{G} = 1.5$) and softest (corresponding to $\hat{G} = 85.5$) responses increasingly diverge from each other with increasing $\hat{\tau}$. While these trends are most clearly seen for $\dot{\epsilon} = 0.03 \text{ s}^{-1}$, they persist for the other two rates albeit to a lesser extent. Moreover, with increasing $\dot{\epsilon}$ the responses for $\hat{\tau} \lesssim 1$ tend to become independent of \hat{G} , they remain distinct for $\hat{\tau} > 1$. As seen from the figure, the model (Eq. (6)) captures these trends very well with the fitted optimal parameters in Fig. 6.

Fig. B.3 collates the rate-dependent porosity evolution for the ranges of material relaxation modulus ratios (\hat{G}) and relaxation time-scale ratios ($\hat{\tau}$). The symbols are finite element results and the lines are analytical results of Eq. (10).

The relation $\epsilon_p = \alpha(\epsilon_c)^n$ prescribed to arrive at Eq. (10) is obtained from the finite element results as illustrated in Fig. B.4 for $\hat{G} = 85.5$; for other \hat{G} ratios the trends are qualitatively similar. In Fig. B.4, for both the regimes of $\hat{\tau}$ the ϵ_p - ϵ_c relationship is nonlinear for all three $\dot{\epsilon}$ values. Beyond the critical cell strain $\epsilon_c = \epsilon_c^{\rm cr}$, which corresponds to $\phi = 0$ the relationship becomes independent of $\dot{\epsilon}$ and $\hat{\tau}$. Similar trends are observed for other \hat{G} ratios.

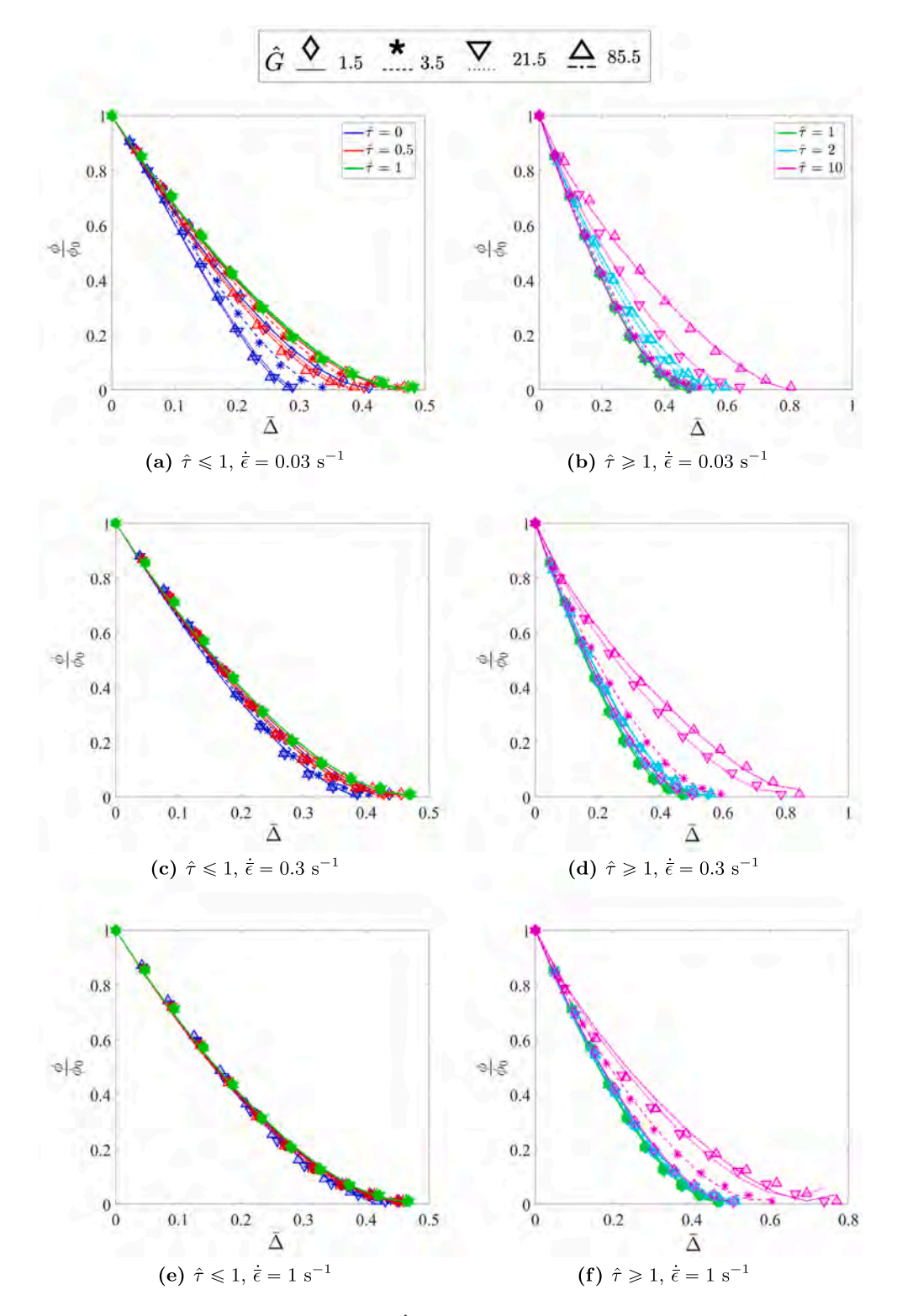


Fig. B.3. Rate-dependent porosity evolution for different $\hat{G} - \hat{\tau}$ combinations. Finite element (symbols) and model (Eq. (10), lines).

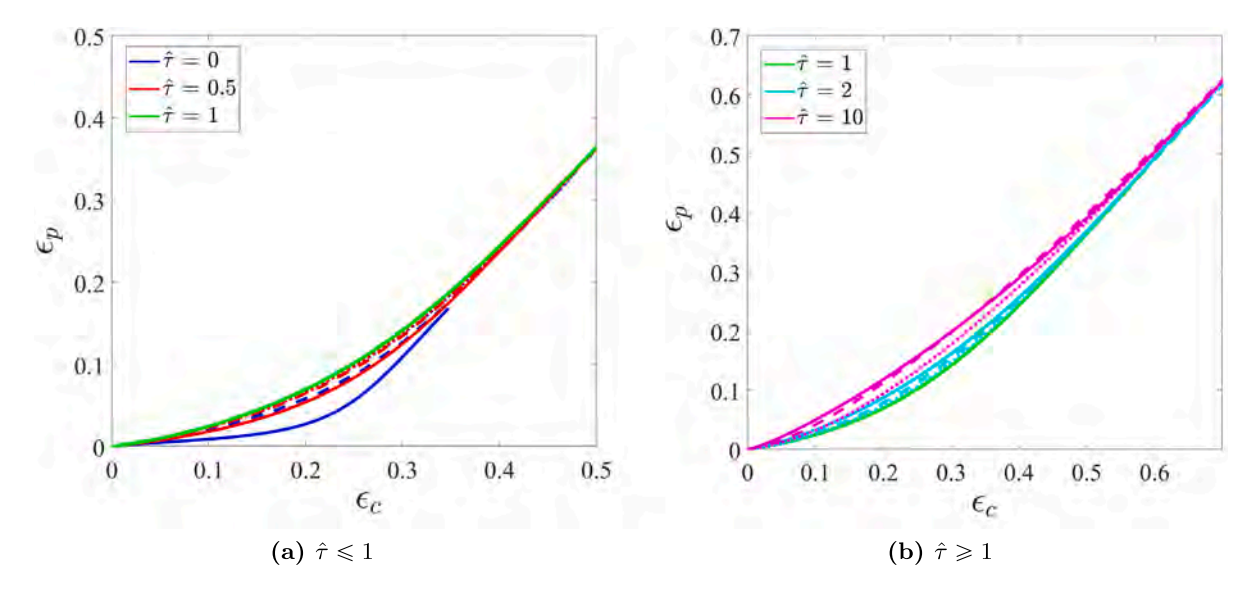


Fig. B.4. Finite element results showing ϵ_p - ϵ_c evolution for $\hat{G}=85.5$ and different $\hat{\tau}-\hat{\epsilon}$ combinations. $\hat{\epsilon}=0.03 \text{ s}^{-1}$ (----), $\hat{\epsilon}=0.3 \text{ s}^{-1}$ (----) and $\hat{\epsilon}=1 \text{ s}^{-1}$ (-----).

Appendix C. Supplementary data

Supplementary material related to this article can be found online at https://doi.org/10.1016/j.jmps.2024.105574.

References

Ashour, A., Trittel, T., Börzsönyi, T., Stannarius, R., 2017. Silo outflow of soft frictionless spheres. Phys. Rev. Fluids 2 (12), 123302.

Ball, J.M., 1982. Discontinuous equilibrium solutions and cavitation in nonlinear elasticity. Philos. Trans. R. Soc. Lond. A 306 (1496), 557-611.

Barber, J.R., 2018. Contact Mechanics, vol. 250, Springer.

Barney, C.W., Dougan, C.E., McLeod, K.R., Kazemi-Moridani, A., Zheng, Y., Ye, Z., Tiwari, S., Sacligil, I., Riggleman, R.A., Cai, S., et al., 2020. Cavitation in soft matter. Proc. Natl. Acad. Sci. 117 (17), 9157–9165.

Bellehumeur, C.T., Kontopoulou, M., Vlachopoulos, J., 1998. The role of viscoelasticity in polymer sintering. Rheol. Acta 37 (3), 270-278.

Brodu, N., Dijksman, J.A., Behringer, R.P., 2015. Spanning the scales of granular materials through microscopic force imaging. Nature Commun. 6 (1), 1–6. Cantor, D., Cárdenas-Barrantes, M., Preechawuttipong, I., Renouf, M., Azéma, E., 2020. Compaction model for highly deformable particle assemblies. Phys. Rev. Lett. 124 (20), 208003.

Chen, H., Trivedi, A., Siviour, C., 2020. Application of linear viscoelastic continuum damage theory to the low and high strain rate response of thermoplastic polyurethane. Exp. Mech. 60, 925–936.

Cohen, W., 1960. Rheological problems of solid-propellant rocketry. In: Plasticity. Elsevier, pp. 568-579.

Cohen, T., Durban, D., 2010. Cavitation in elastic and hyperelastic sheets. Internat. J. Engrg. Sci. 48 (1), 52-66.

Coleman, B.D., Noll, W., 1961. Foundations of linear viscoelasticity. Rev. Modern Phys. 33 (2), 239.

Commins, T., Siviour, C.R., 2023. Stress relaxation after low-and high-rate deformation of polyurethanes. Proc. R. Soc. Lond. Ser. A Math. Phys. Eng. Sci. 479 (2275), 20220830.

Dijksman, J.A., Zheng, H., Behringer, R.P., 2013. Imaging soft sphere packings in a novel triaxial shear setup. In: AIP Conference Proceedings, Vol. 1542, No. 1. American Institute of Physics, pp. 457–460.

Durian, D.J., 1995. Foam mechanics at the bubble scale. Phys. Rev. Lett. 75 (26), 4780.

Eom, Y., Boogh, L., Michaud, V., Sunderland, P., Månson, J.-A., 2001. Stress-initiated void formation during cure of a three-dimensionally constrained thermoset resin. Polym. Eng. Sci. 41 (3), 492–503.

Garoz, D., Gilabert, F., Sevenois, R., Spronk, S., Van Paepegem, W., 2019. Consistent application of periodic boundary conditions in implicit and explicit finite element simulations of damage in composites. Composites B 168, 254–266.

Gent, A., Lindley, P., 1959. Internal rupture of bonded rubber cylinders in tension. Proc. R. Soc. Lond. A 249 (1257), 195-205.

Giannis, K., Schilde, C., Finke, J., Kwade, A., Celigueta, M., Taghizadeh, K., Luding, S., 2021. Stress based multi-contact model for discrete-element simulations. Granul. Matter 23 (2), 1–14.

Gonzalez, M., Cuitiño, A.M., 2012. A nonlocal contact formulation for confined granular systems. J. Mech. Phys. Solids 60 (2), 333-350.

Graham, G., 1967. The contact problem in the linear theory of viscoelasticity when the time dependent contact area has any number of maxima and minima. Internat. J. Engrg. Sci. 5 (6), 495–514.

Grassia, L., D'Amore, A., Simon, S.L., 2010. On the viscoelastic Poisson's ratio in amorphous polymers. J. Rheol. 54 (5), 1009-1022.

Guo, J., Zehnder, A.T., Creton, C., Hui, C.-Y., 2020. Time dependent fracture of soft materials: linear versus nonlinear viscoelasticity. Soft Matter 16 (26), 6163–6179.

Highley, C.B., Song, K.H., Daly, A.C., Burdick, J.A., 2019. Jammed microgel inks for 3D printing applications. Adv. Sci. 6 (1), 1801076.

Hirsch, M., Charlet, A., Amstad, E., 2021. 3D printing of strong and tough double network granular hydrogels. Adv. Funct. Mater. 31 (5), 2005929.

Horabik, J., Molenda, M., 2016. Parameters and contact models for DEM simulations of agricultural granular materials: A review. Biosyst. Eng. 147, 206-225.

Huebsch, N., Lippens, E., Lee, K., Mehta, M., Koshy, S.T., Darnell, M.C., Desai, R.M., Madl, C.M., Xu, M., Zhao, X., et al., 2015. Matrix elasticity of void-forming hydrogels controls transplanted-stem-cell-mediated bone formation. Nature Mater. 14 (12), 1269–1277.

Jagota, A., Argento, C., Mazur, S., 1998. Growth of adhesive contacts for Maxwell viscoelastic spheres. J. Appl. Phys. 83 (1), 250-259.

Jagota, A., Dawson, P., 1988a. Micromechanical modeling of powder compacts—I. Unit problems for sintering and traction induced deformation. Acta Metall. 36 (9), 2551–2561.

Jagota, A., Dawson, P., 1988b. Micromechanical modeling of powder compacts—II. Truss formulation of discrete packings. Acta Metall. 36 (9), 2563–2573. Kabla, A.J., 2012. Collective cell migration: leadership, invasion and segregation. J. R. Soc. Interface 9 (77), 3268–3278.

Karanjgaokar, N., 2017. Evaluation of energy contributions using inter-particle forces in granular materials under impact loading. Granul. Matter 19 (2), 36.

Karpiesiuk, J., 2020. Young's modulus and Poisson's ratio of polyurethane adhesive in lightweight floor system. Modern Approaches Mater. Sci. 2 (3), 251–255.

Kocharyan, H., Karanjgaokar, N., 2020. Influence of lateral constraints on wave propagation in finite granular crystals. J. Appl. Mech. 87 (7), 071011.

Leaderman, H., 1958. Rheology, vol. 2, Academic Press, New York.

Lefèvre, V., Ravi-Chandar, K., Lopez-Pamies, O., 2015. Cavitation in rubber: an elastic instability or a fracture phenomenon? Int. J. Fract. 192, 1-23.

Li, L., Karapiperis, K., Andrade, J.E., 2021. Emerging contact force heterogeneity in ordered soft granular media. Mech. Mater. 162, 104055.

Lin, S., Mao, Y., Radovitzky, R., Zhao, X., 2017. Instabilities in confined elastic layers under tension: Fringe, fingering and cavitation. J. Mech. Phys. Solids 106, 229–256.

Lopez-Pamies, O., 2009. Onset of cavitation in compressible, isotropic, hyperelastic solids. J. Elasticity 94, 115-145.

Lubliner, J., 1985. A model of rubber viscoelasticity. Mech. Res. Commun. 12 (2), 93-99.

Makse, H.A., Johnson, D.L., Schwartz, L.M., 2000. Packing of compressible granular materials. Phys. Rev. Lett. 84 (18), 4160.

McMeeking, R.M., Jefferson, G., Haritos, G.K., 2001. Elastic and visco-elastic response of finite particle junctions in granular materials. Nato Sci. Ser. Sub Ser. Iii Comput. Syst. Sci. 176, 50–62.

Menut, P., Seiffert, S., Sprakel, J., Weitz, D.A., 2012. Does size matter? Elasticity of compressed suspensions of colloidal-and granular-scale microgels. Soft Matter 8 (1), 156–164.

Mukhopadhyay, S., Peixinho, J., 2011. Packings of deformable spheres. Phys. Rev. E 84 (1), 011302.

Nakhatakyan, F., 2011. Precise solution of hertz contact problem for circular cylinders with parallel axes. Russian Eng. Res. 31 (3), 193-196.

Oberth, A., Bruenner, R., 1965. Tear phenomena around solid inclusions in castable elastomers. Trans. Soc. Rheol. 9 (2), 165-185.

O'hern, C.S., Silbert, L.E., Liu, A.J., Nagel, S.R., 2003. Jamming at zero temperature and zero applied stress: The epitome of disorder. Phys. Rev. E 68 (1), 011306.

Raps, D., Hossieny, N., Park, C.B., Altstädt, V., 2015. Past and present developments in polymer bead foams and bead foaming technology. Polymer 56, 5–19. Riley, L., Schirmer, L., Segura, T., 2019. Granular hydrogels: emergent properties of jammed hydrogel microparticles and their applications in tissue repair and regeneration. Curr. Onin. Biotechnol. 60, 1–8.

Shireen, Z., Hajizadeh, E., Daivis, P., Brandl, C., 2023. Linear viscoelastic shear and bulk relaxation moduli in poly(tetramethylene oxide) (PTMO) using united-atom molecular dynamics. Comput. Mater. Sci. 216, 111824.

Shull, K.R., 2002. Contact mechanics and the adhesion of soft solids. Mater. Sci. Eng. R 36 (1), 1-45.

Simo, J.C., 1987. On a fully three-dimensional finite-strain viscoelastic damage model: formulation and computational aspects. Comput. Methods Appl. Mech. Engrg. 60 (2), 153–173.

Simo, J.C., Hughes, T.J., 2006. Computational Inelasticity, vol. 7, Springer Science & Business Media.

Tang, Y., Kang, J., Wang, Y.Q., 2022. Cavity expansion in nonlinear viscoelastic solids: A nonlinear dynamic study. Int. J. Non-Linear Mech. 144, 104076.

Theocaris, P., 1965. Relaxation response of polyurethane elastomers. J. Polymer Sci. A 3, 2619–2635.

van Hecke, M., 2009. Jamming of soft particles: geometry, mechanics, scaling and isostaticity. J. Phys.: Condens. Matter 22 (3), 033101. Vu, T.-L., Barés, J., Mora, S., Nezamabadi, S., 2019. Numerical simulations of the compaction of assemblies of rubberlike particles: A quantitative comparison with experiments. Phys. Rev. E 99 (6), 062903.

Vu, T.-L., Nezamabadi, S., Mora, S., 2021. Effects of particle compressibility on structural and mechanical properties of compressed soft granular materials. J. Mech. Phys. Solids 146, 104201

Wineman, A., 2009. Nonlinear viscoelastic solids—a review. Math. Mech. Solids 14 (3), 300-366.

Xu, D., Ji, C., Munjiza, A., Kaliviotis, E., Avital, E., Willams, J., 2019. Study on the packed volume-to-void ratio of idealized human red blood cells using a finite-discrete element method. Appl. Math. Mech. 40 (5), 737–750.

Yee, A., Takemori, M., 1982. Dynamic bulk and shear relaxation in glassy polymers. I. Experimental techniques and results on PMMA. J. Polymer Sci. Polymer Phys. Ed. 20, 205–224.

Yuk, H., Wu, J., Sarrafian, T.L., Mao, X., Varela, C.E., Roche, E.T., Griffiths, L.G., Nabzdyk, C.S., Zhao, X., 2021. Rapid and coagulation-independent haemostatic sealing by a paste inspired by barnacle glue. Nat. Biomed. Eng. 5 (10), 1131–1142.

Zhang, B., Yuan, C., Zhang, W., Dunn, M.L., Qi, H.J., Liu, Z., Yu, K., Ge, Q., 2019. Recycling of vitrimer blends with tunable thermomechanical properties. RSC Adv. 9 (10), 5431–5437.

Zheng, Y., Cai, S., 2020. Analytical solutions of cavitation instability in a compressible hyperelastic solid. Int. J. Non-Linear Mech. 126, 103562.